2012

# Load Reduction of Floating Wind Turbines using Tuned Mass Dampers

Gordon M. Stewart
*University of Massachusetts Amherst*

# LOAD REDUCTION OF FLOATING WIND TURBINES USING TUNED MASS DAMPERS

A Thesis Presented

by

GORDON M. STEWART

Submitted to the Graduate School of the
University of Massachusetts Amherst in partial fulfillment
of the requirements for the degree of

MASTER OF SCIENCE IN MECHANICAL ENGINEERING

February 2012

Mechanical Engineering

# LOAD REDUCTION OF FLOATING WIND TURBINES USING TUNED MASS DAMPERS

A Thesis Presented

by

GORDON M. STEWART

Approved as to style and content by:

Matthew Lackner, Chair

Sanjay Arwade, Member

James Manwell, Member

Donald Fisher, Department Chair
Mechanical Engineering

# ABSTRACT

## LOAD REDUCTION OF FLOATING WIND TURBINES USING TUNED MASS DAMPERS

FEBRUARY 2012

GORDON M. STEWART

B.Sc., UNIVERSITY OF MASSACHUSETTS AMHERST

M.S.M.E., UNIVERSITY OF MASSACHUSETTS AMHERST

Directed by: Professor Matthew Lackner

Offshore wind turbines have the potential to be an important part of the United States' energy production profile in the coming years. In order to accomplish this wind integration, offshore wind turbines need to be made more reliable and cost efficient to be competitive with other sources of energy. To capitalize on high speed and high quality winds over deep water, floating platforms for offshore wind turbines have been developed, but they suffer from greatly increased loading. One method to reduce loads in offshore wind turbines is the application of structural control techniques usually used in skyscrapers and bridges. Tuned mass dampers are one structural control system that have been used to reduce loads in simulations of offshore wind turbines. This thesis adds to the state of the art of offshore wind energy by developing a set of optimum passive tuned mass dampers for four offshore wind turbine platforms and by quantifying the effects of actuator dynamics on an active tuned mass damper design.

The set of optimum tuned mass dampers are developed by creating a limited degree-of-freedom model for each of the four offshore wind platforms. These models

are then integrated into an optimization function utilizing a genetic algorithm to find a globally optimum design for the tuned mass damper. The tuned mass damper parameters determined by the optimization are integrated into a series of wind turbine design code simulations using FAST. From these simulations, tower fatigue damage reductions of between 5 and 20% are achieved for the various TMD configurations.

A previous study developed a set of active tuned mass damper controllers for an offshore wind turbine mounted on a barge. The design of the controller used an ideal actuator in which the commanded force equaled the applied force with no time lag. This thesis develops an actuator model and conducts a frequency analysis on a limited degree-of-freedom model of the barge including this actuator model. Simulations of the barge with the active controller and the actuator model are conducted with FAST, and the results are compared with the ideal actuator case. The realistic actuator model causes the active mass damper power requirements to increase drastically, by as much as 1000%, which confirms the importance of considering an actuator model in controller design.

# TABLE OF CONTENTS

# LIST OF TABLES

**Table** **Page**

# LIST OF FIGURES

**Figure** **Page**

# CHAPTER 1

# INTRODUCTION

Offshore wind turbines have the potential to be a significant contributor to global energy production, due to the proximity of the high quality wind resource to coastal energy loads. However, due to the addition of wave and current loads, offshore structures must be made stronger, and thus more expensive than their land based counterparts. The reliability of offshore turbines suffers due to the higher loading, and the inaccessibility of the turbines for maintenance compounds this problem. The ability to reduce loads is therefore extremely important for offshore wind turbines, as it allows for increased reliability and possibly lighter and cheaper structures [31].

In order to access offshore winds far offshore over deeper water, floating platforms for wind turbines are being designed and studied. With few water depth and sea floor restrictions, these platforms could be placed anywhere in the oceans with suitable electricity transmission. Also, since the platforms can be towed by boats, the wind turbines could be moved or brought to shore for maintenance. Floating wind turbines, however, have been shown to experience much higher fatigue and ultimate loading than onshore or fixed bottom offshore turbines, and could therefore benefit greatly from load reduction techniques.

One method to reduce loading is to utilize structural control systems, which have been used successfully in civil structures to achieve improved structural response [32, 40]. For civil structures, the main purpose of structural control systems is increased inhabitant comfort by reducing building accelerations, but this reduced acceleration also leads to reduced fatigue loading. In wind turbine applications, fatigue is a design

driver. While fixed bottom offshore platforms can benefit from structural control due to reduced fatigue damage, floating platforms experience increased motion due to relative platform flexibility and any reduction in these motions should result in a significant decrease in fatigue. The application of these systems to offshore wind turbines is the subject of this Master's research. Specifically, the thesis develops models and tools to design, analyze and optimize both passive and active structural control systems for floating and fixed bottom offshore wind turbines.

In the first chapter, a review of the literature explains the background of the problem. The state of offshore wind research is discussed which will review the offshore foundations and platforms used in the studies in this thesis. The wind turbine design code, FAST, is introduced. Civil engineering applications of structural control are outlined, reviewing the different types of structural control. Finally, the literature on the integration of structural control and offshore wind turbines is presented.

The second chapter investigates the work on the optimization of a passive tuned mass damper (TMD) for four offshore platforms. The goal of this chapter is to identify the best passive system for load reduction. First a limited degree of freedom structural model of each platform is created, then this model is used as an objective function for a genetic algorithm. The genetic algorithm is used to find the TMD spring and damper that provides either the largest tower fatigue reduction, or the largest mooring line fatigue reduction, depending on the specific design drivers of the platform used. Once the optimum TMDs are found, a series of high fidelity simulations is run for each platform using a modification to the National Renewable Energy Laboratory (NREL) wind turbine design code, FAST. These simulations quantify the improvement that each TMD design has over the baseline system.

Chapter 3 presents research on the active tuned mass damper. A previous study had developed an active controller for the barge floating platform, but an actuator model was excluded from the system identification and simulations [33]. The active

structural control literature stresses that inclusion of an actuator model is important in obtaining a robust controller because the actuator adds dynamics to the system. Without the actuator model, the original active controller may not be viable, so this chapter seeks to determine the effect of adding a realistic actuator. After developing a mathematic model of an electric motor to be used as the actuator, a frequency analysis is conducted on the system. The frequency analysis helps to provide a thorough understanding of the problem of control structure interaction. Finally, full degree of freedom FAST simulations are run for cases with and without the actuator model for comparison.

# CHAPTER 2

# LITERATURE REVIEW

This chapter will take an in-depth look at the literature surrounding offshore wind turbines as well as structural control. Throughout the review, problems or gaps in the state of the art will be identified and used as motivation for the work done in this thesis.

## 2.1 Offshore Wind

As onshore wind reaches a state of relative technical maturity, more offshore wind farms are being built. The low turbulence, high speed wind resource offshore is another benefit. Figure 2.1 shows the onshore wind resource map for the United States. The wind speeds are taken at a height of 80 meters. It can be seen from this map that most of the onshore wind resource is in the interior of the country, in areas of low population density and far from many of the major load centers on the coasts. Figure 2.2 shows the offshore wind resource. Not only are the wind speeds higher, but the high wind speeds regions are larger and more uniform. Also, the offshore wind resource is closer to the coastal population, which reduces electricity transmission distances. Offshore wind turbines also may be able to achieve more efficient designs due to a higher noise tolerance. Without the stringent noise requirements of onshore turbines, turbines can have higher tip speed ratios, which in general leads to more efficient turbine designs.

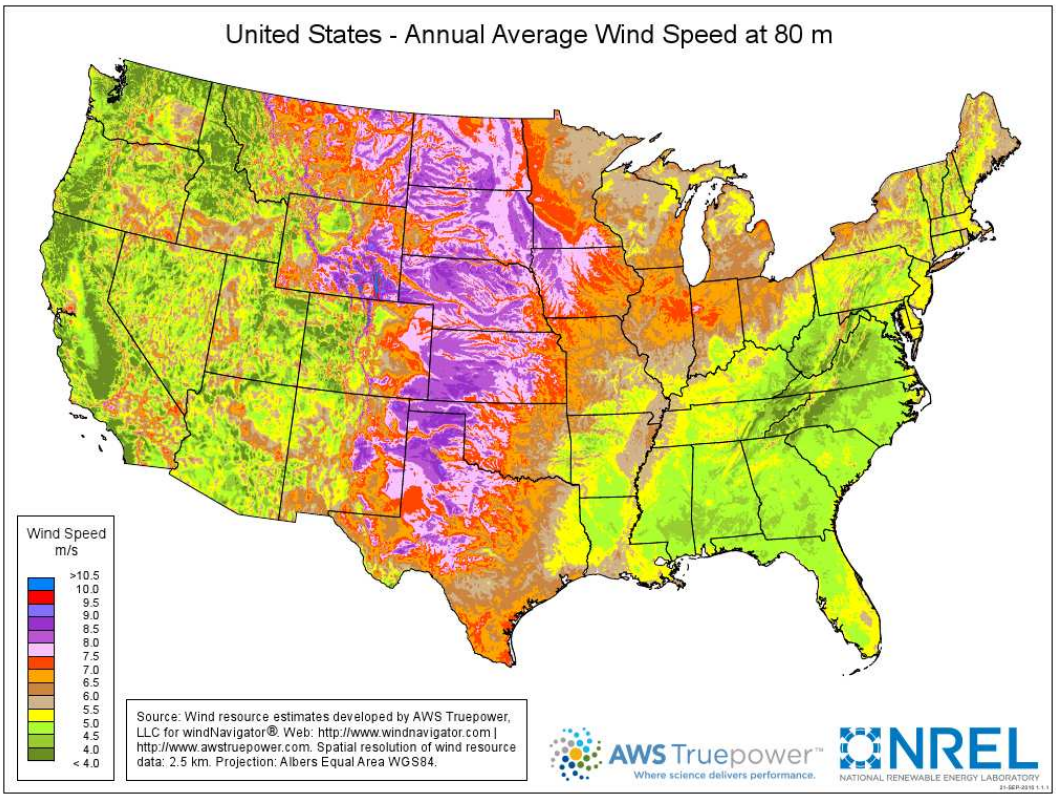


**Figure 2.1.** Onshore wind resource at 80m height for the United States

### 2.1.1 Properties of Offshore Wind Turbines

Wind turbine sizes have been changing dramatically over the past 40 years. Figure 2.3 from the European Wind Energy Association (EWEA) shows the increase in the size of the diameters of installed wind turbines.

Figure 2.3 covers both on land and offshore wind turbines, and the trend toward large turbines is more pronounced for offshore turbines. This is due to the costs associated with constructing and installing the foundations or platforms for offshore turbines. Figure 2.4 shows the construction of an offshore wind turbine.

This research uses a representative 5 MW wind turbine model developed by NREL. This is a three bladed upwind machine with a 90m hub height and a 126m rotor

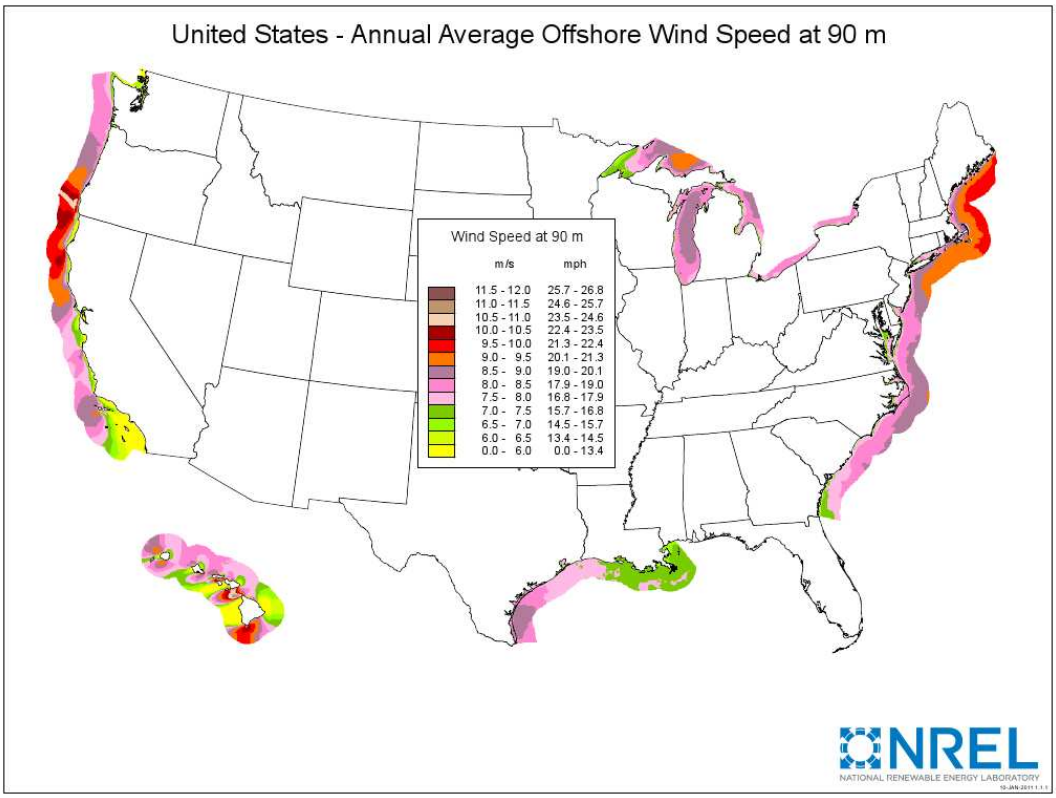


**Figure 2.2.** Offshore wind resource at 90m height for the United States

diameter [20]. Table 2.1 outlines other properties of the turbine. The baseline control includes variable speed operation and collective blade pitch control. This turbine is used for many research efforts as it provides a common model for comparison between studies.

There are a few additional engineering challenges that must be addressed to make offshore wind turbines (OWTs) more viable. Both floating and fixed bottom OWTs require a more expensive foundation than land based turbines. The addition of wave and current loading on the turbine coupled with the added flexibility of the offshore floating platform or fixed bottom foundation is an important engineering problem. With the additional loading and flexibility, the components of OWTs, particularly

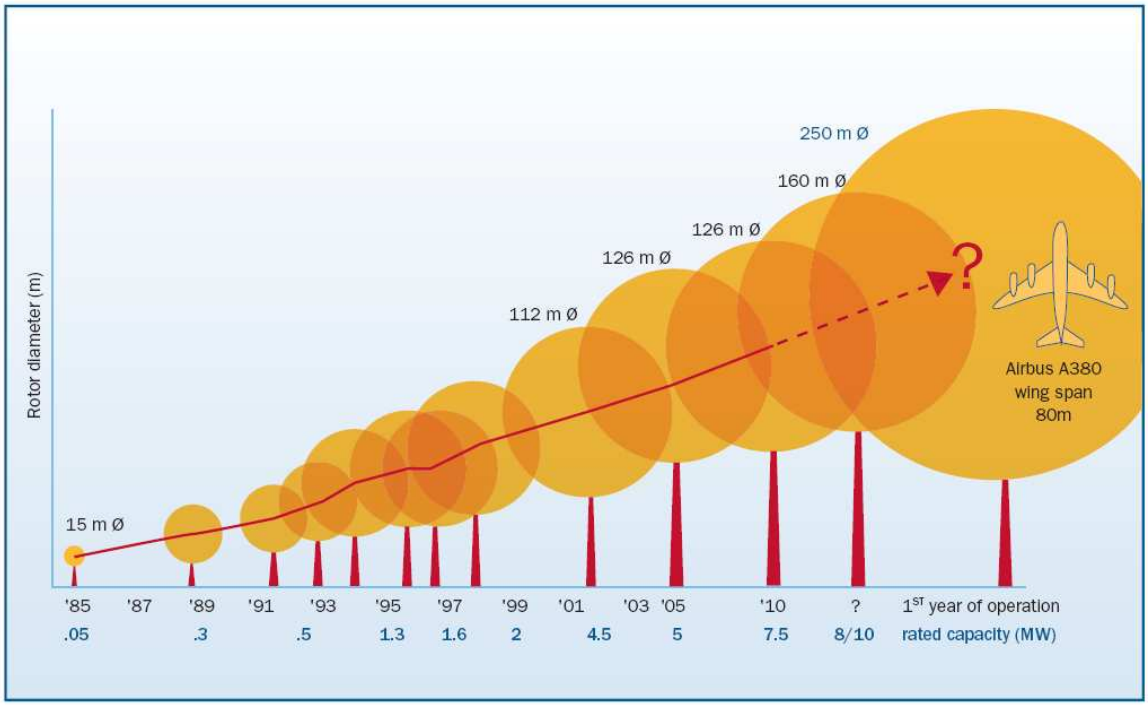


**Figure 2.3.** Advances in wind turbine size [11].

the towers and blades, must be made stronger and heavier, which increases the cost. Boats are required in order to maintain the components of OWTs, which increases operation and maintenance costs as well. All of these factors combine to make fixed bottom offshore wind turbines up to 2-3 times more expensive than onshore wind turbines, and floating turbines even more expensive. Reducing the effects of the additional loading on OWTs has the potential to reduce these elevated costs.

For the purposes of this thesis, there are two broad categories of offshore wind turbine platforms, fixed bottom and floating. Both categories are further divided into foundation types. Fixed bottom structures include monopiles, jacket foundations, gravity foundations, and vacuum piles. For floating platforms, the designs include buoyancy stabilized barges, ballast stabilized spar buoys, and mooring line stabilized tension-leg platforms. See Figure 2.5 for a depiction of feasible depth ranges for the

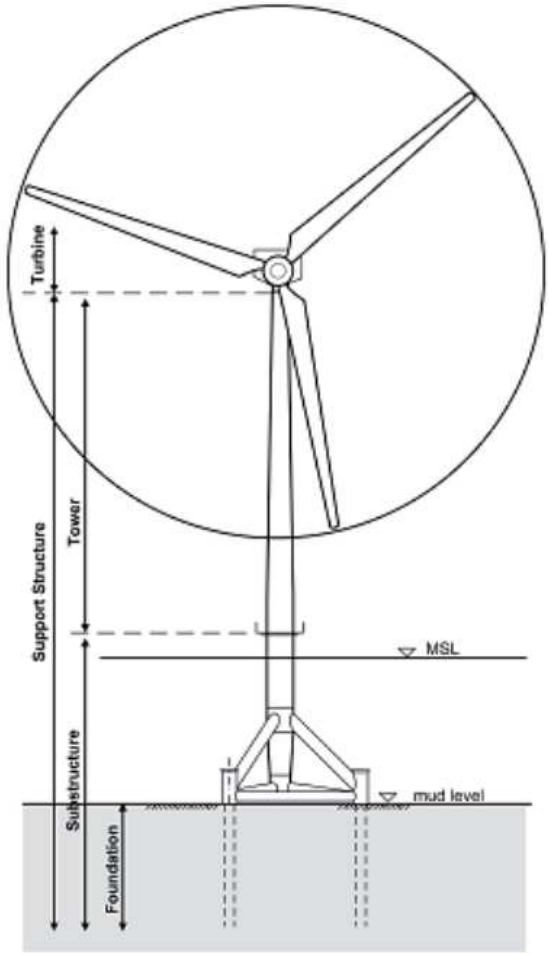


**Figure 2.4.** Offshore wind turbine terminology [15]

various platforms designs [31]. The features of all of these designs will be discussed in the following sections.

### 2.1.2 Fixed Bottom Offshore Wind Turbines

All of the power producing offshore wind turbines in the world today use fixed bottom foundations. These structures are highly dependent on ocean floor conditions, as well as water depth. Different types of fixed bottom foundations have been developed in order to expand the locations suitable for installation, which are categorized

| | |
|---|---|
| Rating | 5 MW |
| Rotor Orientation, Configuration | Upwind, 3 Blades |
| Control | Variable Speed, Collective Pitch |
| Drivetrain | High Speed, Multiple-Stage Gearbox |
| Rotor, Hub Diameter | 126 m, 3 m |
| Hub Height | 90 m |
| Cut-In, Rated, Cut-Out Wind Speed | 3 m/s, 11.4 m/s, 25 m/s |
| Cut-In, Rated Rotor Speed | 6.9 rpm, 12.1 rpm |
| Rated Tip Speed | 80 m/s |
| Overhang, Shaft Tilt, Precone | 5 m, 5, 2.5 |
| Rotor Mass | 110,000 kg |
| Nacelle Mass | 240,000 kg |
| Tower Mass | 347,460 kg |
| Coordinate Location of Overall CM | (-0.2 m, 0.0 m, 64.0 m) |
| Nacelle Dimensions | 18 m x 6 m x 6 m |

**Table 2.1.** Physical Parameters of NREL 5MW Baseline Turbine [20]

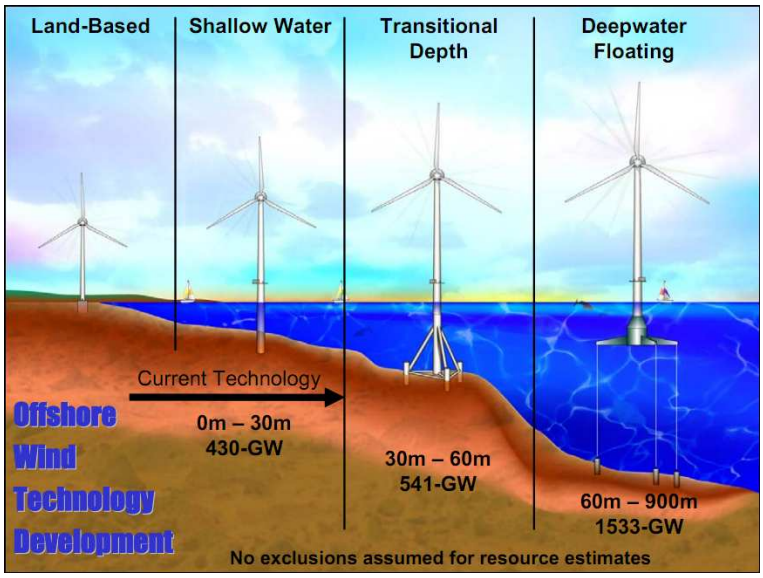


**Figure 2.5.** Depth ranges for proposed and existing offshore wind turbine foundation designs [31].

by water depth in this thesis. The following sections will define and give examples for both shallow water and transitional depth foundations.

#### 2.1.2.1 Shallow Water Foundations

Wind turbines that are installed in up to approximately 30 meters of water are considered shallow water foundations [31]. The main three foundation types for shallow water are the monopile, the gravity base, and the suction bucket. These foundations are depicted in Figure 2.6 The monopile consists of a steel hollow tube that is driven

**Figure 2.6.** Three shallow water wind turbine foundations; the monopile, the gravity base, and the suction bucket from right to left [31].

down into the seabed, with a transitional piece attaching the pile to the tower of the turbine. The gravity base uses a large heavy slab, usually concrete, on the ocean floor for its support. The suction bucket, also known as a suction caisson, uses a shorter but wider tube than the monopile, but the tube is evacuated of all water after installation, providing a suction force that gives stability to the turbine. All three of these foundations are highly dependent on seabed conditions. The monopile needs the ocean floor to be soft enough to allow the pile to go deep enough, but also firm enough to provide lateral support under tower loading. Gravity bases have problems with non-homogeneous soil settling, which could cause the turbine to angle over. The

suction caisson needs certain kinds of soil to maintain the partial vacuum that gives the structure its support.

The most common shallow water foundation that is used today is the monopile due to its relative simplicity and small environmental footprint. Therefore, a monopile will be used in this research as the representative fixed bottom foundation. The specific monopile used is a standard design from NREL that can be simulated by the FAST turbine design code. This monopile is a 6m diameter hollow steel tube that is simulated in 20m of water.

#### 2.1.2.2 Transitional Depth Foundations

In transition water depths between 30 and 60 m, a different class of fixed bottom foundations are used, as the shallow water foundations just discussed are no longer feasible. There are a multitude of proposed foundations for this depth, which can be seen in Figure 2.7. These foundations are as follows (from left to right): tripod tower,

**Figure 2.7.** Transitional water depth foundation designs. [31].

guyed monopole, full-height jacket, submerged jacket with transition to tube tower, and enhanced suction bucket or gravity base [31]. This research will not utilize any transitional depth turbines, but they are included here for reference.

### 2.1.3 Floating Wind Turbines

Floating wind turbines have the potential to be placed anywhere in the ocean from 60 meters to upwards of 900 m or beyond. This is a great benefit, because floating platforms allow offshore wind penetration into places where it may be prohibitive for fixed bottom offshore turbines. These places include the Great Lakes and the west coast of the United States where there is little shallow water. Floating platforms are also much less dependent on seabed conditions than fixed bottom structures because they do not rely on the ocean floor for support, with mooring line anchors being a notable exception. Many of the floating platform designs are able to be towed by boats in order to be moved relatively easily. This may reduce costs associated with construction and maintenance. See Figure 2.8 for a qualitative chart comparing costs from different offshore wind turbines.

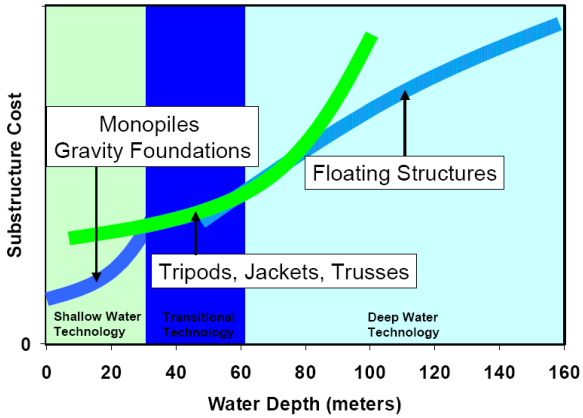


**Figure 2.8.** Cost comparison of various offshore wind turbine platform designs [31].

Floating platforms lose the stiffness associated with the fixed ground foundations, and gain new degrees of freedom. The naming convention for the floating platforms' degrees of freedom used in this thesis can be seen in Figure 2.9. This thesis uses three different floating platforms designs. The three major sources of stability for floating platforms are buoyancy, ballast, and mooring line tension. Each platform uses

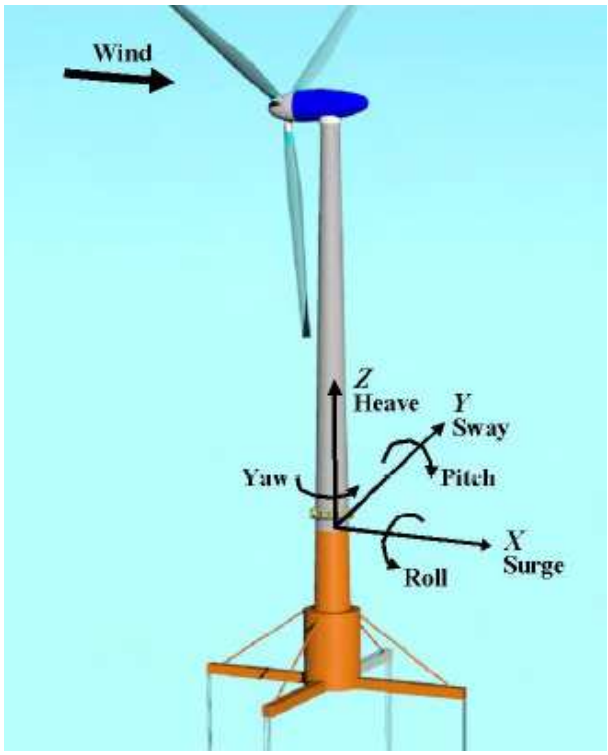


**Figure 2.9.** Naming and sign conventions for the 6 platform DOFs [17].

some combination of these three stability sources, with one source being dominant. Figure 2.10 shows a diagram of how different platform designs achieve stability. The

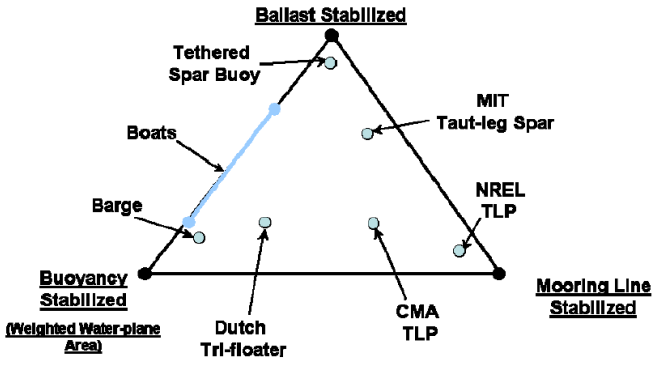


**Figure 2.10.** Scatter plot showing how different platform designs acheive stability [5].

platforms used in this research are the ITI Energy Barge, the OC3-Hywind Spar Buoy,

and the NREL Tension-Leg Platform. As Figure 2.10 shows, the barge depends mostly on buoyancy, the spar buoy mostly on ballast, and the tension-leg platform mostly on mooring line tension.

#### 2.1.3.1 ITI Energy Barge

The ITI Energy barge is a floating platform designed by the Department of Naval Architecture and Marine Engineering at the Universities of Glasgow and Strathclyde through a contract with ITI Energy [17]. This platform was originally designed to be used with the NREL 5 MW turbine. The barge has eight catenary mooring lines, two coming off each corner. The lines are added to tether the barge in place, but also provide some stiffness. A graphic of the barge with the NREL 5MW mounted on it can be seen in Figure 2.11 [21]. A table referencing important physical parameters of the barge is in Table 2.2.

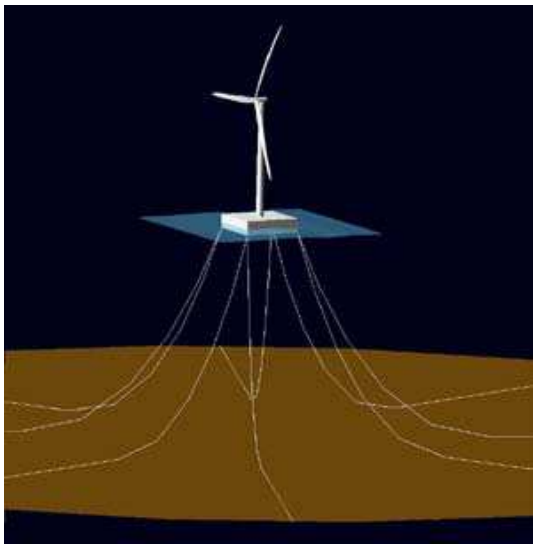

**Figure 2.11.** Graphic depicting the ITI Energy Barge

There are a few problems with the design of the ITI Energy Barge. The pitching mode has a natural frequency close to the peak frequency of a typical wave spectrum, and thus is significantly excited by wave loading. This excitation causes high loading

on the tower in the fore-aft direction, which is discussed more in Section 2.1.3.4. The barge is one of the simplest of the floating platforms to construct, and it is also relatively easy to tow from a construction site near the shore to the turbine site. These attributes make it an attractive platform, but the high tower loading must be addressed.

| | MIT/NREL TLP | OC3-Hywind Spar Buoy | ITI Energy Barge |
|---|---|---|---|
| Diameter or width × length | $18m$ | $6.5 to 9.4m$ (is tapered) | $40m \times 40m$ |
| Draft | $47.89m$ | $120m$ | $4m$ |
| Water displacement | $12,180m^3$ | $8,029m^3$ | $6,000m^3$ |
| Mass, including ballast | $8.6 \times 10^6 kg$ | $7.47 \times 10^6 kg$ | $5.45 \times 10^6 kg$ |
| CM location below still water level (SWL) | $40.61m$ | $89.92m$ | $0.2818m$ |
| Roll inertia about CM | $5.72 \times 10^8 kg \cdot m^2$ | $4.23 \times 10^9 kg \cdot m^2$ | $7.27 \times 10^8 kg \cdot m^2$ |
| Pitch inertia about CM | $5.72 \times 10^8 kg \cdot m^2$ | $4.23 \times 10^9 kg \cdot m^2$ | $7.27 \times 10^8 kg \cdot m^2$ |
| Yaw inertia about CM | $3.61 \times 10^8 kg \cdot m^2$ | $1.64 \times 10^8 kg \cdot m^2$ | $1.45 \times 10^9 kg \cdot m^2$ |
| Number of mooring lines | $8(4 pairs)$ | 3 | 8 |
| Depth to fairleads, anchors | $47.89m, 200m$ | $70m, 320m$ | $4m, 150m$ |
| Radius to fairleads, anchors | $27m, 27m$ | $5.2m, 853.9m$ | $28.28m, 423.4m$ |
| Unstretched line length | $151.7m$ | $902.2m$ | $473.3m$ |
| Line diameter | $0.127m$ | $0.09m$ | $0.0809m$ |
| Line mass density | $116kg/m$ | $77.71kg/m$ | $130.4kg/m$ |
| Line extensional stiffness | $1.5 \times 10^9 N$ | $3.84 \times 10^8 N$ | $5.89 \times 10^8 N$ |

**Table 2.2.** Table showing the parameters of the three floating platforms [21].

#### 2.1.3.2 OC3-Hywind Spar Buoy

A Norway based company, StatoilHydro, developed a spar buoy design that is currently supporting a Siemens 2.3 MW turbine in a floating demonstration project, the Hywind project. NREL modified this design to be compatible with the NREL 5MW turbine, and the result is called the OC3-Hywind Spar Buoy. Figure 2.12 shows the design, and physical properties of the platform can be seen in Table 2.2. The spar buoy uses a heavy counterbalance at the base of the spar to move the center of mass below the center of buoyancy. This creates a restoring moment if the spar is pitched or rolled. This design lacks stiffness in the yaw DOF however, which could cause substantial off-axis wind flow.

**Figure 2.12.** Graphic depicting the OC3-Hywind Spar Buoy

#### 2.1.3.3 MIT/NREL Tension-Leg Platform

The MIT/NREL Tension-Leg Platform (TLP) is a joint design by MIT and NREL. This platform uses four legs with 2 taut mooring lines on each leg to provide a restoring force. The central spar part of the TLP is weighted on the bottom, which adds stiffness and also makes it possible for the platform to be towed without the lines or turbine attached. A depiction of the platform can be seen in Figure 2.13, and properties are once again listed in Table 2.2. This platform is very stiff in pitch and roll due to the tendons, but it lacks stiffness in surge and sway. Mooring line fatigue and ultimate loads become a driving factor in the design of this platform due to the potentially catastrophic situation that would result from a mooring line failure.

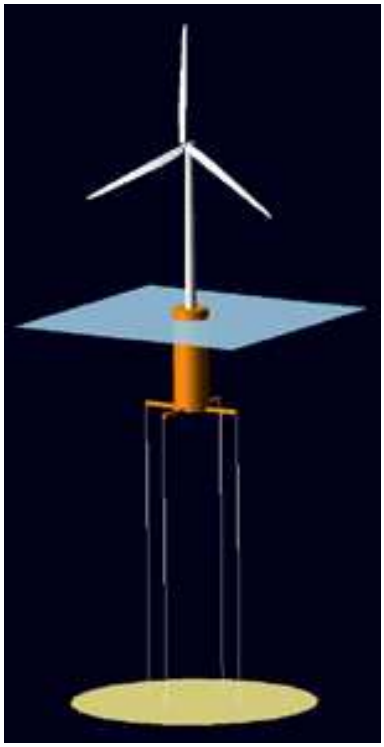

**Figure 2.13.** Graphic depicting the MIT/NREL TLP

#### 2.1.3.4 Floating Platform Comparison

All three platforms have relative advantages and disadvantages. The TLP has better load reduction characteristics, it is more expensive to manufacture and harder to site due to the anchors needed. The spar buoy has medium performance in loading, has the largest mass of material involved in construction, but is fairly simple. The barge has the worst load performance, but is relatively simple to manufacture.

In one study, fatigue loads were compared in identical wind and wave conditions using FAST [21]. The results from this study can be seen in Figure 2.14. For all of the platforms, tower fore-aft bending fatigue was at least 50% greater than the land based turbine. The spar and barge had fatigue damage of up to 2.5 and 8 times greater than the land turbine, respectively. The side-side tower fatigue loading is

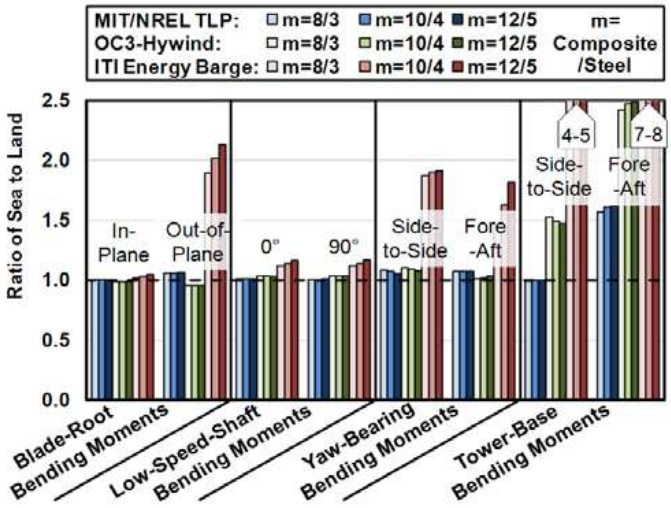


**Figure 2.14.** Fatigue damage on various components of the three floating platform designs [21].

also higher for the floating platforms. This increase in fatigue damage is the main motivating factor of the entire thesis, which is aimed at trying to reduce this loading.

## 2.2 Structural Control

Structural control is the civil engineering discipline that uses dynamic systems to reduce acceleration and loading in buildings and bridges due to wave and earthquake forcing. There are many different designs for the systems used to accomplish this goal ranging from massive pendulums to precisely controlled servomotor mass dampers. For over twenty years, numerous large-scale active and passive structural control systems have been implemented for civil structures [1, 2, 22, 34, 36, 37]. The following section will outline passive, semi-active, and active structural control.

### 2.2.1 Passive Structural Control

The simplest type of structural control devices are passive, which use no power to operate. As the structure vibrates, some of the vibrational energy is transfered to the

mass of the structural control device and dissapated by the damper. Sections 2.2.1.1 & 2.2.1.2 will outline the designs of passive structural control devices.

#### 2.2.1.1 Passive Tuned Mass Dampers

The most common passive structural control device is the tuned mass damper (TMD). This device utilizes a mass on an ideally frictionless track. The TMD mass and the main structure are connected via a spring and dashpot. In the ideal form of the TMD, both of these components are linear and have a constant spring and damping constant. The mass and spring are tuned to a system frequency that causes loading, which results in the TMD mass vibrating at this frequency. The damper then dissipates energy from the whole system in the form of heat. The theory is simple, but tuning the spring and damping constants optimally can be difficult. Even for an idealized one degree of freedom structure, the optimal tuning for the spring and damper is dictated by a complex function [23]. For structures with more degrees of freedom and nonlinearities like an offshore wind turbine, there is no analytical solution for the optimal tuning, and numerical approaches must be used. Figure 2.15 shows a diagram of a tuned mass damper.

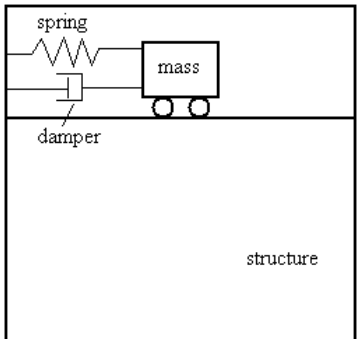


**Figure 2.15.** Schematic of a Passive TMD

#### 2.2.1.2 Other Passive Structural Control Designs

Alternative passive devices have been utilized besides the simple mass on a track just discussed. These include tuned liquid dampers (TLDs), tuned liquid column dampers (TLCDs), and pendulum dampers. Tuned liquid dampers use the sloshing of a fluid to provide a force on the structure, while TLCDs improve upon this idea by using two attached vertical columns of liquid with an orifice between them to provide the damping force [13, 29]. The difference between the heights of the two liquid columns provides an equivalent spring force, and the fluid passing through the orifice provides a damping force. Pendulum dampers use the swinging of a large pendulum tuned to a certain frequency to provide a counter-force to structural accelerations. Figure 2.16 & 2.17 show these two dampers.

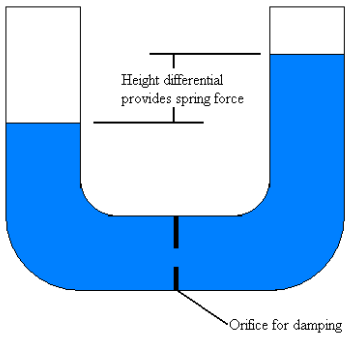


**Figure 2.16.** Schematic tuned liquid column damper

### 2.2.2 Semi-Active Structural Control

Semi-active mass damper (SAMD) utilize a damper that can change its damping constant during operation. This ability can be used to tune the mass damper on the fly and can result in better performance compared to passive TMDs with a minimal energy investment when compared to active dampers (see Section 2.2.3) [34, 38]. The damper in these systems can take the form of an electrorheological (ER), magnetorheological (MR), or fluid viscous damper [35–37]. The ER and MR dampers use

**Figure 2.17.** Pendulum damper from the Taipei101 tower.

either an electric or magnetic field respectively to change the viscosity of the fluid in the damper. The fluid viscous damper uses a controlled valve to vary the viscous resistance through the damper orifice [38]. Figure 2.18 shows a fluid viscous damper, and Figure 2.19 shows an electrorheological damper.

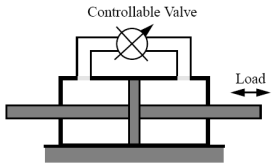


**Figure 2.18.** Diagram of controllable valve damper

### 2.2.3 Active Structural Control

Active structural control devices use a controlled actuator in order to apply forces to the mass and structural and potentially have an even greater impact on structural acceleration than passive and semi-active systems. Active systems can operate over

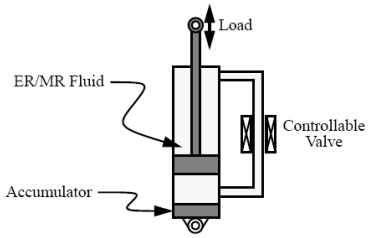


**Figure 2.19.** Schematic of electrorheological damper.

a wider frequency band, and can apply higher forces to the structure by way of the actuator.

#### 2.2.3.1 Active Mass Damper

An active mass damper (AMD) consists of a mass and an actuator, which can be actively controlled to apply a force to the mass and an equal and opposite force on the structure [3, 9, 14, 34]. Since there is no physical spring and damper in this system, the actuator must provide all of the forces to the mass damper. There is also the potential to destabilize the system and add energy to the structure if the control scheme is not well designed.

#### 2.2.3.2 Hybrid Mass Damper

The HMD combines the TMD and AMD, and features both a tuned mass, spring, and damper system as well as an actuator [35, 37]. With the addition of an actuator, the HMD gains the potential for improved performance over a passive system. Examples of installed HMDs utilizing servomotor and hydraulic actuators can be found in the literature [12, 40]. Both the AMD and HMD can add energy to the system, thus there is a potential for instability. The HMD, however, includes a passive system, so it can still provide load reduction with no actuation power.

#### 2.2.3.3 Control Structure Interaction

In practical applications of active structural control, it is critical to understand and account for the dynamics of the actuator when modeling and designing the overall system. Control-structure interaction (CSI) refers to the dynamic interaction between the structure and the actuator in active structural control applications, and is an unavoidable result of using a real actuator for generating active control forces. Control-structure interaction exists because there is a natural feedback path between the structure and the actuator. This feedback can be seen in the block diagram in Figure2.20 [8]. Note that in addition to the effect of the actuator on the structure (indicated by "f" in Figure2.20), there is also an influence on the actuator by the structure. In the past, control systems for structures neglected CSI, which can severely limit performance and robustness [4, 8].

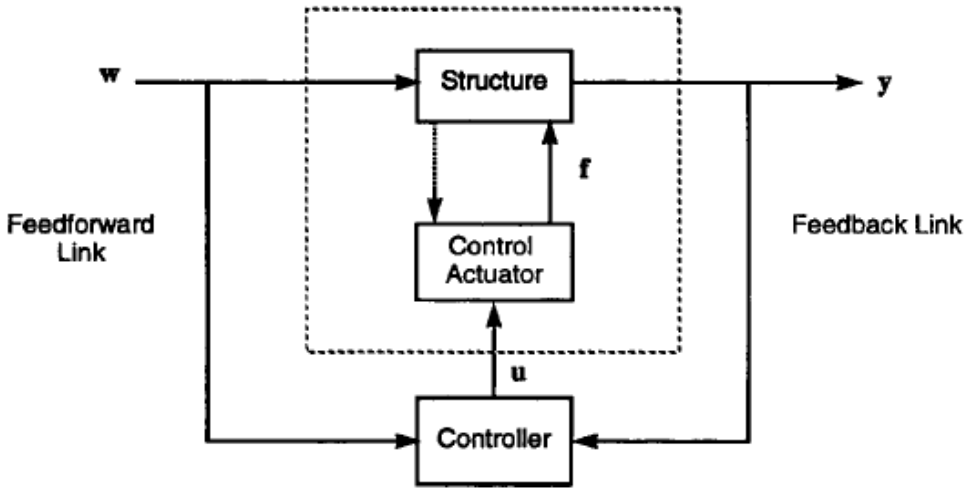


**Figure 2.20.** Block diagram showing CSI [8]

## 2.3 Structural Control in Offshore Wind

### 2.3.1 Passive Structural Control in Offshore Wind Turbines

Research has been conducted on using passive TMDs for wind turbines, especially for offshore structures due to the larger loading [6, 7, 10, 30, 39]. Earlier studies focused on fixed bottom structures, but previous work also focused on floating structures [26, 28]. This research led to the development of FAST-SC, an updated version of the NREL wind turbine aero-elastic design code, which has the capability to simulate both passive and active tuned mass dampers. More details on the capabilities of the FAST-SC code are discussed below, and can be found in the literature [27, 28, 33].

FAST is a fully coupled aero-hydro-servo-elastic code that simulates the performance of wind turbines [19]. It uses Blade Element-Momentum theory (BEM) or generalized dynamic wake theory to calculate aerodynamic loads, a linear modal representation for structural components, and a non-linear hydrodynamic subroutine that calculates wave loading on the platform for offshore applications [16]. This code is interfaced through Matlab/Simulink, and a controller can be implemented graphically with Simulink.

A modification to FAST to accommodate structural control (FAST-SC) was developed by Lackner and Rotea [28]. This code includes the capability to model two independent TMDs, one in the fore-aft direction and one in the side-side direction (see Figure 2.21). The TMDs can be located in the nacelle or the platform. The addition of locating the TMD in platform is mainly for the spar buoy and TLP platforms, in which it may be desired to move the TMD into the platform. This layout is attractive because there is little room in the nacelle for extraneous systems like the TMD, and since extra mass in the nacelle could create unwanted loading. It may also be feasible to use a larger TMD in the platform than in the nacelle, which could increase performance. In addition to the spring and damping forces, an active force provided by an actuator can be applied to the mass [27, 33]. Position constraints known as stops

are imposed on the stroke of the TMDs. These constraints were introduced because the nacelle has a limited amount of space, but the stops can be set to any distance.

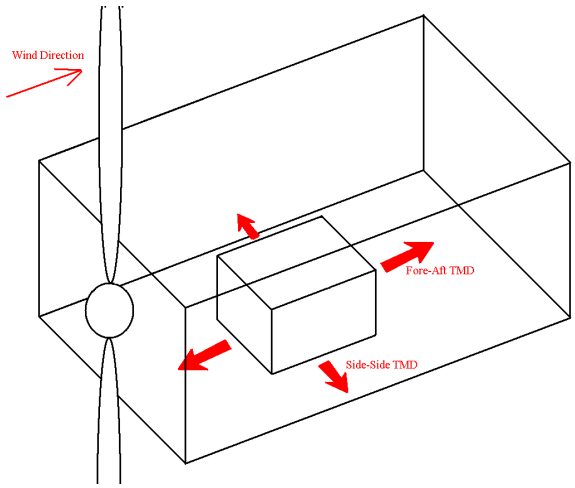


**Figure 2.21.** Diagram showing direction of Fore-Aft and Side-Side TMDs in a nacelle.

In the research of Lackner et al., a passive TMD was tuned for the ITI Energy Barge and the monopile. A parametric study was used to find the optimum spring and damping constants. The spring constant was chosen by finding the system natural frequency that was dominant in causing tower bending and tuning the TMD spring constant for a given mass to match that frequency. The damping constant was then found by running FAST-SC with a range of different values and determining the decrease in tower bending for each value. From this, the near optimum damping constant was found for that specific spring constant. This approach has a few problems however. First, it was assumed that the spring constant that matches the system natural frequency is optimum. Further research shows this is not necessarily the case, especially in nonlinear systems like a wind turbine [23, 24]. Also, the optimization scheme is limited to only the damping values selected in the parametric study.

### 2.3.2 Active Structural Control in Offshore Wind Turbines

Previous work [27, 33] developed a set of active controllers for an HMD system in the NREL 5MW offshore wind turbine [20] using a barge for the platform model. The HMD was located in the nacelle of the turbine in the fore-aft orientation (see Fig 2.21), with a mass of $20,000kg$. Using 4% of the rated turbine power for the actuator, the tower damage load was reduced by up to 20% over the optimal passive system, and 28-33% compared to the baseline system. However, there are practical limitations to the spring length, and the turbine HMD has a much longer stroke than is common in systems in civil structures. For this reason, it may be necessary to use an AMD configuration rather than an HMD. Also, the past research used an ideal actuator model. With this model, the force that the controller demanded was applied instantly to the mass and nacelle, and thus actuator dynamics were ignored.

## 2.4 Problems Addressed and Contributions to the State of the Art

After a review of the literature surrounding the use of structural control in offshore wind, this thesis will address the following important research topics:

- A more thorough analysis and design of a passive tuned mass damper will be conducted for all four of the offshore platforms: the monopile, barge, spar buoy, and tension leg platform, discussed above in Section 2.1.3. This research will seek to identify the optimum configuration of a passive tuned mass damper for each of respective platforms in an attempt to reduce tower fatigue and mooring line fatigue. With a comprehensive set of simulations encompassing different platform designs and TMD locations, masses and orientations, a quantitative assessment of the relative performance of passive tuned mass dampers will be made.

- The effects of introducing a more realistic actuator model into the current active control design for Rotea et al will be addressed in Chapter 4 [33]. According to the literature on control structure interaction, the addition of a realistic actuator changes how the controller should be designed, and if this is not considered it could lead to a sub-optimum or worse, an unstable system. This research will develop and analyze a more realistic simulation of the active controller system for the barge. The results for this simulation will be compared to previous results from the active controller, and suggestions will be made for future work for the controller.

# CHAPTER 3

# PASSIVE TUNED MASS DAMPER OPTIMIZATION

In this chapter, the work on the optimization of a passive TMD for each of the four platforms is discussed. First, a limited degree of freedom model is designed for each platform configuration. Next, an optimization scheme is employed in order to optimize the spring and damping constants for the TMD. Finally, the optimum TMD configurations are run through a series of FAST-SC simulations in order to compare their performance to the baseline case with no TMD.

## 3.1 Limited Degree of Freedom Offshore Turbine Models

The ideal way to optimize the TMD parameters would be to create a function that would wrap an optimization scheme around FAST-SC, which would pick a spring and damping constant, simulate the system in FAST-SC, and then modify the parameters in order to get closer to the minimum of some output from FAST-SC, for example, tower fatigue. However, the simulation time for a 10 minute FAST-SC simulation is approximately 10-30 minutes, and the optimization scheme could potentially need thousands of function calls to find an optimum. Also, in the case of the offshore platforms used in this study, there is usually a single system degree of freedom that is responsible for the most fatigue loading, so FAST-SC is overkill in terms of computations needed. Therefore, in order to quickly and efficiently find the optimum TMD configuration for each platform, a limited degree of freedom model is constructed from the basic equations of motion. For the monopile, barge and spar, minimization of tower base fatigue loading is the objective function, and for the TLP, both tower

fatigue and mooring line fatigue are considered. These models are built to capture the degrees of freedom for the specific platform that are the source of most of the loading.

### 3.1.1 Monopile Limited DOF Model

The monopile is the simplest of the models; there are only 2 degrees of freedom that are a concern, the tower bending DOF and the TMD DOF. Since the fore-aft direction has the highest loading from wind and waves, this direction has the highest tower fatigue damage. For this reason, the following models consider the for-aft direction, but side-side modeling is possible with minor modifications. The tower is modeled as an inverted pendulum with the structural stiffness and damping modeled as a rotary spring and rotary damper at the base of the rigid body, and the TMD is modeled as a simple mass on a linear track with a linear spring and damper. A diagram of the model can be seen in Figure 3.1.

In this figure, the $k$ terms are spring constants, the $d$ terms are damping constants, and the $m$ terms are masses. The $t$ subscripts represent the tower degree of freedom and the $tmd$ subscripts are for the TMD. The angle that the tower has bent from vertical is denoted by $\theta_t$, and the displacement of the TMD from is shown as $x_{tmd}$. After applying a simple dynamic analysis as well as small angle approximations to the two degrees of freedom, Equations 3.1 & 3.2 are found. Small angle approximations are appropriate because in simulations, none of the platforms exceed 10 degrees of pitch, even in the heaviest wind and wave loadings.

$$\begin{aligned} I_t\ddot{\theta}_t = {} & m_t g R_t \theta_t - k_t\theta_t - d_t\dot{\theta}_t - k_{tmd}R_{tmd}(R_{tmd}\theta_t - x_{tmd}) \\ & - d_{tmd}R_{tmd}(R_{tmd}\dot{\theta}_t - \dot{x}_{tmd}) - m_{tmd}g(R_{tmd}\theta_t - x_{tmd}) \end{aligned} \tag{3.1}$$

$$\begin{aligned} m_{TMD}\ddot{x}_{TMD} = {} & k_{TMD}(R_{TMD}\theta_t - x_{TMD}) + d_{TMD}(R_{TMD}\dot{\theta}_t - \dot{x}_{TMD}) \\ & + m_{TMD}g\theta_t \end{aligned} \tag{3.2}$$

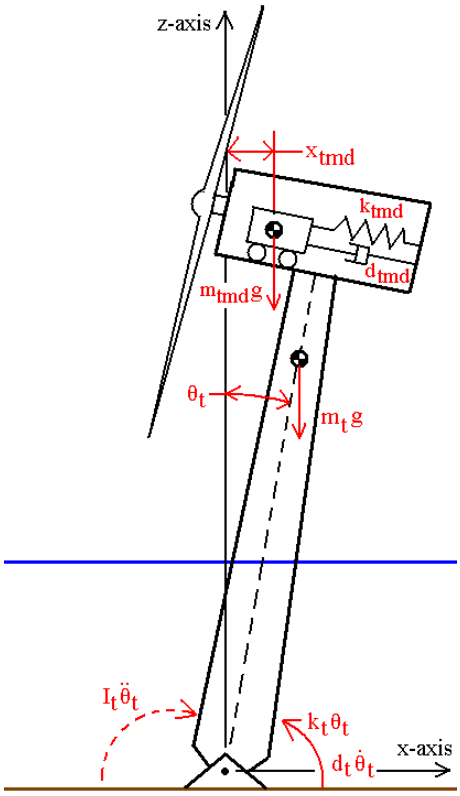


**Figure 3.1.** Diagram of the limited degree-of-freedom model for the monopile.

The R terms are the distances from the tower hinge to the center of mass of the degree of freedom indicated by the subscript. For example, $R_{tmd}$ is the distance from the tower hinge to the center of mass of the TMD. All of the degrees of freedoms in the models are in a global reference frame. Thus, $x_{tmd}$ is not defined relative to the position in the nacelle, but rather from the global zero which can be seen in Figure 3.1 as the z-axis. If the nacelle has moved 1 meter to the right, and the TMD has moved 1 meter to the right in the nacelle, then $x_{tmd}$ would equal 2 meters. This modeling choice is made so there are no inertial terms from other degrees of freedom in any of the equations, which simplifies the implementation of the model (see Section 3.2).

### 3.1.2 Barge

The barge must be modeled with an additional degree of freedom to account for the compliance of the floating platform. It has been shown in other studies that the pitching degree of freedom for the barge causes the most tower bending [18]. Therefore, the model includes the tower and TMD degrees of freedom, and also has a pitching degree of freedom. This model can be seen in Figure 3.2. Equations 3.3-3.5

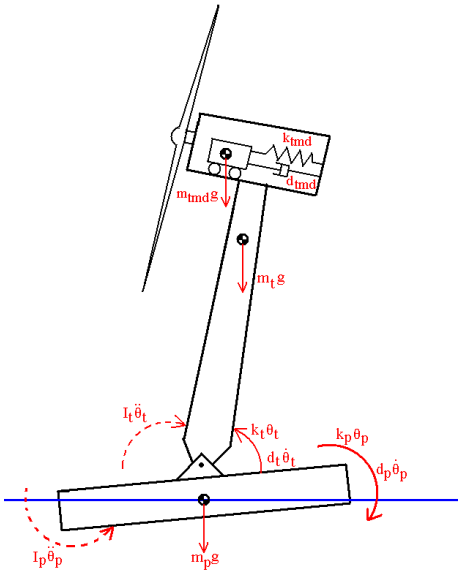


**Figure 3.2.** Diagram of the limited degree-of-freedom model for the barge.

show the equations for the platform, tower, and TMD.

$$I_p\ddot{\theta}_p = -d_p\dot{\theta}_p - k_p\theta_p - m_pgR_p\theta_p + k_t(\theta_t - \theta_p) + d_t(\dot{\theta}_t - \dot{\theta}_p) \tag{3.3}$$

$$\begin{aligned} I_t\ddot{\theta}_t = {} & m_tgR_t\theta_t - k_t(\theta_t - \theta_p) - d_t(\dot{\theta}_t - \dot{\theta}_p) - k_{TMD}R_{TMD}(R_{TMD}\theta_t - x_{TMD}) \\ & - d_{TMD}R_{TMD}(R_{TMD}\dot{\theta}_t - \dot{x}_{TMD}) - m_{TMD}g(R_{TMD}\theta_t - x_{TMD}) \end{aligned} \tag{3.4}$$

$$m_{TMD}\ddot{x}_{TMD} = k_{TMD}(R_{TMD}\theta_t - x_{TMD}) + d_{TMD}(R_{TMD}\dot{\theta}_t - \dot{x}_{TMD}) + m_{TMD}g\theta_t \tag{3.5}$$

The subscripts and variables in these equations are the same as in the Equations 3.1 & 3.2, with the addition of the "p" subscript for the platform DOF. The spring constant of the barge, $k_p$, represents a summation of hydrostatic restoring moments and mooring line stiffness. The barge damping constant, $d_p$, includes many sources of hydrodynamic damping, including wave radiation and viscous damping. These terms are non-linear, so the assumption of a linear damping constant adds some inaccuracies to the model. Once again, the angles and displacement are in absolute coordinates so the equations include only one inertial term. The R parameters are from the hinge to the center of mass of the corresponding DOF. In all of the models, the choice of the hinge point as a reference is arbitrary, but it is convenient because the corresponding distances from this point are straightforward to calculate from the given dimensions of the platforms.

### 3.1.3 Spar

The spar buoy model is very similar to the barge, except with this platform, it may make sense to put the TMD in the spar itself, which may have to be widened for the TMD to fit. In order to analyze both the nacelle-based and platform-based TMDs, two models are developed for the spar buoy. Once again, pitch is the platform degree of freedom that causes the most tower bending, so it is the DOF included in the model. Figure 3.3 shows the two models for the spar. There are different sets of equations for the spar with the TMD in the nacelle and the TMD in the platform. For the spar with the TMD in the nacelle, the equations are identical to the barge equations, it is only the parameters themselves that change. With the TMD in the spar, the equations can be seen in Equations 3.6-3.8.

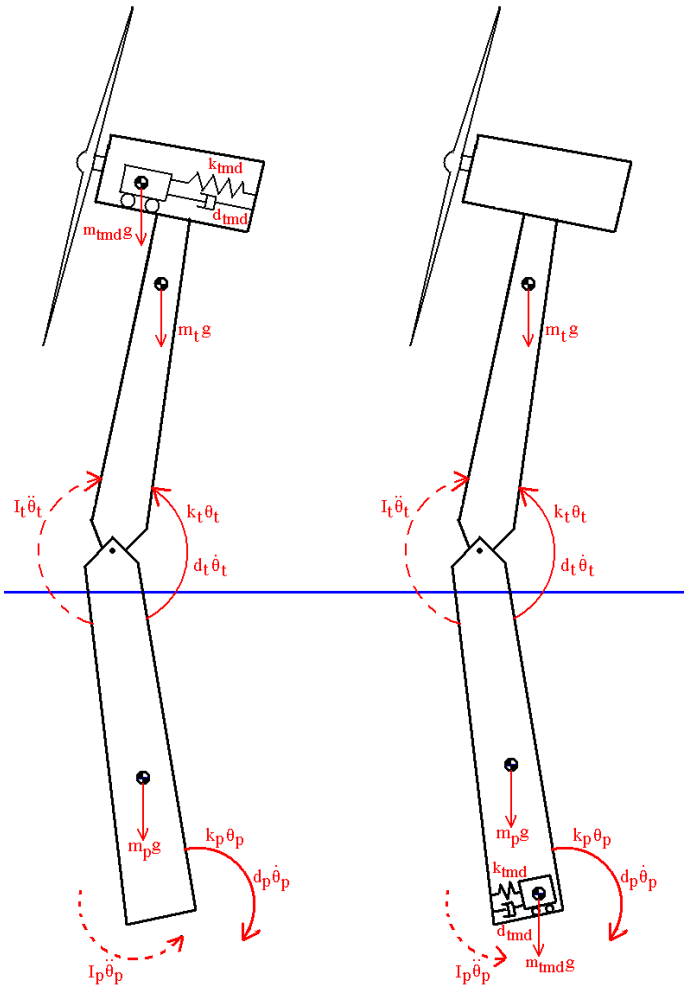


**Figure 3.3.** Diagram of the limited degree-of-freedom model for the spar with the TMD in the nacelle and in the spar.

$$\begin{aligned} I_p\ddot{\theta}_p = & -d_p\dot{\theta}_p - k_p\theta_p - m_p g R_p\theta_p + k_t(\theta_t - \theta_p) + d_t(\dot{\theta}_t - \dot{\theta}_p) \\ & - k_{tmd}R_{tmd}(R_{tmd}\theta_p - x_{tmd}) - d_{tmd}R_{tmd}(R_{tmd}\dot{\theta}_p - \dot{x}_{tmd}) \\ & + m_{tmd}g(R_{tmd}\theta_p - x_{tmd})) \end{aligned} \tag{3.6}$$

$$I_t\ddot{\theta}_t = m_t g R_t\theta_t - k_t(\theta_t - \theta_p) - d_t(\dot{\theta}_t - \dot{\theta}_p) \tag{3.7}$$

$$m_{TMD}\ddot{x}_{TMD} = k_{TMD}(R_{TMD}\theta_p - x_{TMD}) + d_{TMD}(R_{TMD}\dot{\theta}_p - \dot{x}_{TMD}) + m_{TMD}g\theta_p \tag{3.8}$$

Most of the spar buoy's stiffness in pitch comes from the ballast term, which is the $m_p g R_p \theta_p$ term. The spring constant term for the spar buoy represents the effect of the mooring lines and the flotation. Since the flotation force is in the upward direction, the spring constant in this case gives a destabilizing moment to the spar, so it shows up as a negative constant in the equation. The terms in Equation 3.4 & 3.5 that describe the interaction between the tower and the TMD have switched to terms in Equation 3.6 & 3.8 that describe the interaction between the TMD and the platform.

### 3.1.4 TLP

For the tension leg platform, the dominant mode of the system in terms of platform motion is surge; the translational motion into and out of the wind. The TLP undergoes cycles on the order of a few meters in surge, and it is relatively stiff for other degrees of freedom, so this platform motion was initially chosen as the modeling degree of freedom. However, it was found that while the surge motion is the largest in term of magnitude, it was not the cause of most of the tower bending or mooring line fatigue. Instead, pitch was identified as the "problem" degree of freedom, so models for both pitch and surge were built. Furthermore, both a nacelle and platform based TMD are feasible for the pitch model, while only a platform based TMD makes sense for the surge DOF. Figure 3.4 shows the three models used.

These three models show the configuration of the TLP model, but the mathematical model could not be as easily constructed due to a problem with the coupling of the DOFs of the TLP. Due to the taut mooring lines, this platform is different than the other platforms because the lines couple the degrees of freedom. For example, assuming the lines do not stretch (a justifiable assumption since the lines stretch very little relative to the platform motions), if the TLP surges, it must also pitch and

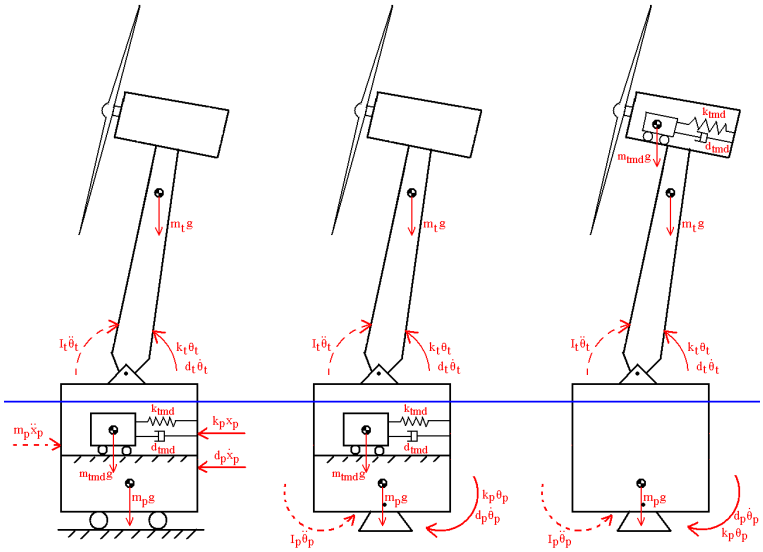


**Figure 3.4.** Diagram of the limited degree-of-freedom model for the surging TLP, the pitching TLP with the TMD in the platform, and the pitching TLP with the TMD in the nacelle, from left to right.

heave to maintain the length of the lines. This relationship can be seen in Figure 3.5, although it is exaggerated in the figure.

This issue can also be seen in a FAST-SC simulation. In the following simulation, only the platform degrees of freedom for the TLP were turned on, and there was no wind or wave loading. The input was a 2 meter surge initial displacement. Figure 3.6 shows surge, pitch and heave from this simulation. The coupling is clear for surge and pitch, as the surging causes pitching at the same frequency due to the effect described in Figure 3.5.

When one tries to isolate one platform degree of freedom like in the monopile, barge, and spar models, the result is an unrealistic model due to the missing coupling effects. An important consequence of this coupling is that if the platform is forced to only surge, the mooring lines are stretched more than they would if the platform could also pitch and heave. This puts large forces on the platform and changes the effective spring constant of the surging motion, which changes the natural frequency of the

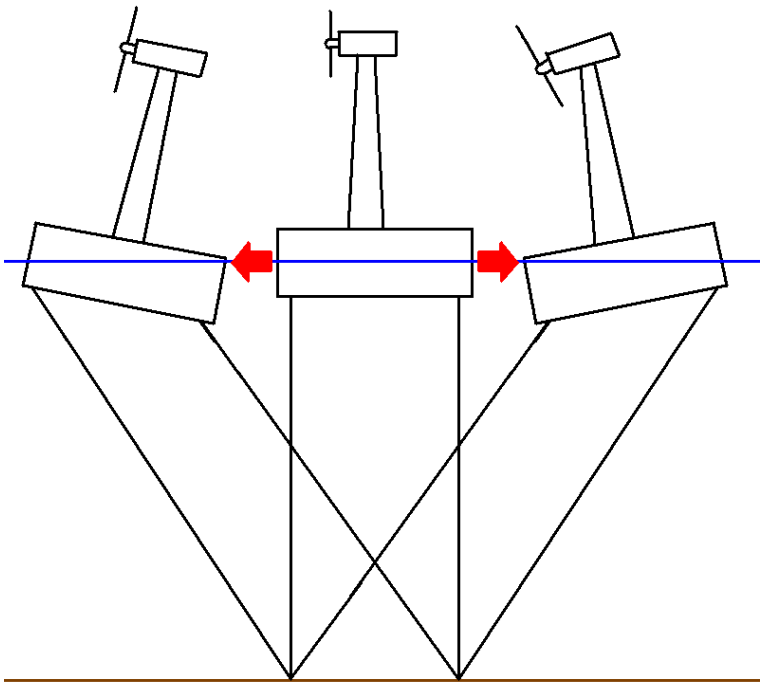

**Figure 3.5.** Diagram showing surge/pitch/heave coupling in TLP due to mooring lines (Exaggerated for effect)

motion. However, trying to include all of the relevant degrees of freedom results in a much more complex model and loses the clarity of the single platform DOF models. For these reasons, a different optimization strategy is used for the TLP that will be explained in Section 3.4.3.

## 3.2 Model Implementation and Tuning

With the mathematical models determined, the equations are then implemented in Simulink. After solving each of the Equations 3.1-3.8 for the acceleration terms, the equations are put into embedded function blocks. The output of these block is the degree of freedom acceleration, which can be integrated twice to get velocity and position. The velocity and position are fed back into the acceleration equation as inputs. The Simulink model showing these main blocks can be seen in Figure 3.7.

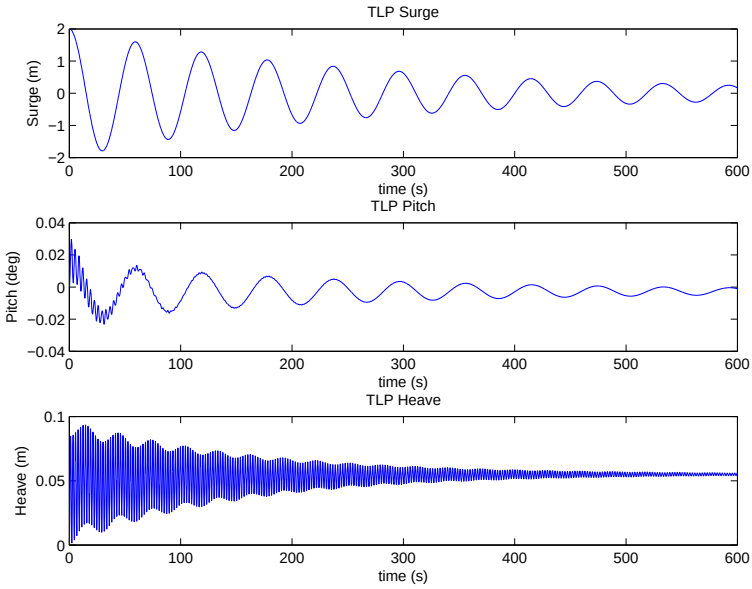


**Figure 3.6.** FAST-SC simulation output showing surge/pitch/heave coupling

In order to use the models to optimize the TMD, the model parameters and the loading must be determined. For all of the platforms, the platform inertia, tower inertia, platform mass, and tower mass can be determined from the FAST-SC input files. The distance terms, $R_p$ and $R_t$ are determined by the center of mass location in relation to the base of the tower, and can be calculated from the platform and tower input files as well. The platform and tower spring and damping constants, however, need to be found by comparing the model to FAST-SC outputs. By applying the same input conditions to the model and a FAST-SC simulation, the outputs can be compared and a non-linear least squares algorithm can determine the spring and damping constants that give the best fit for the model. For the simulations, a step input of tower deflection was used for the monopile, and an initial platform pitch displacement was used for the barge and spar buoy. No wave or wind loading was applied, and the only degrees of freedom that were turned on in FAST-SC were the two or three DOFs in the model. The displacements of the tower and platform degrees of freedom were used as performance metrics, and the least squares algorithm was

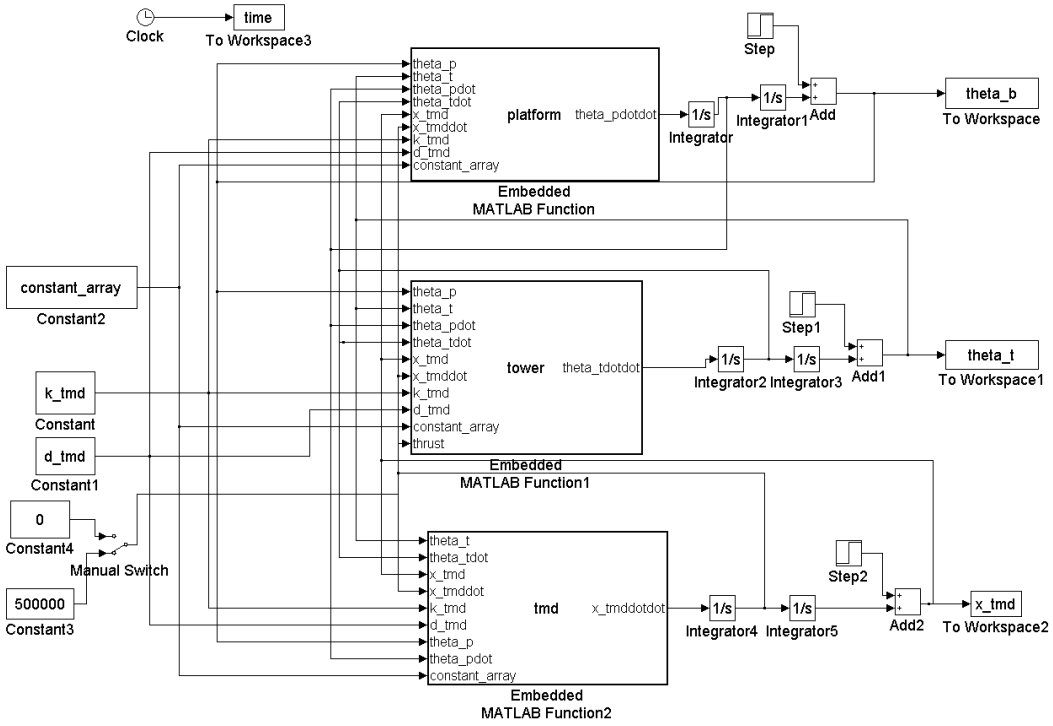


**Figure 3.7.** Simulink Model of Limited Degree of Freedom Model

used to fit the output of the model to the the output of FAST-SC. All platform models had a good agreement with the FAST-SC output using this tuning technique. Figure 3.8 shows the a plot of the fit for the barge model as an example.

The barge pitch angle starts at 5° and oscillates at a frequency of approximately 0.08 Hz, and the damping attenuates the signal throughout the 100s simulation. The second plot is the tower top displacement, which is the amount of tower bending in meters measured at the top of the tower. Tower top displacement (TTD) is relative to the platform coordinate system, so if the platform is pitched but the tower is not bent, then the TTD is zero. In this graph, both the tower and barge pitch frequencies are apparent. The fit between the FAST-SC output and the model output is close, the differences can be attributed to non-linearities in the barge pitch damper and spring in FAST-SC.

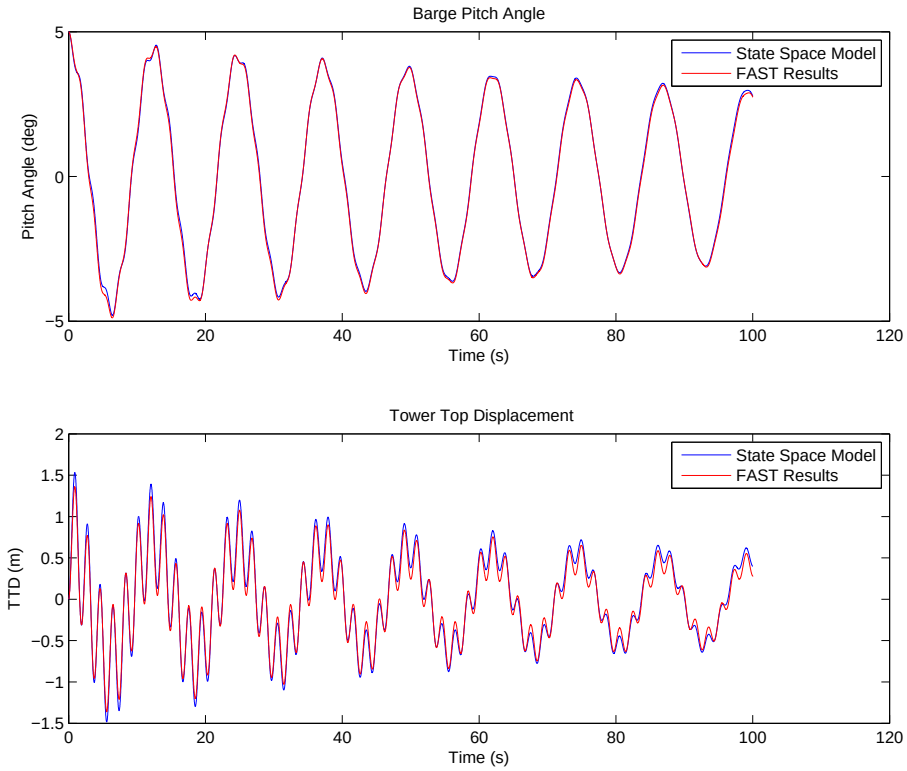


**Figure 3.8.** Figure showing agreement between limited DOF model and FAST with no TMD

### 3.2.1 Realistic Model Loading

With all of the parameters identified for the models, the loading must be chosen for the optimization function. For the actual turbine, the loading is a complex combination of stochastic wind and wave loading. Originally, the model loading for the optimization was the simple step input used in the parameter identification. However, it was found that this gave inaccurate results due to the fact that the thrust force caused by the wind has a non-zero mean. This essentially creates a constant heeling over for some of the platforms, specifically the spar buoy, which changes the parameters of the optimum TMD. The solution is to use a combination of a constant thrust moment on the tower degree of freedom and a pitch step input. The magnitude

of the thrust force is the average of the thrust force from a FAST-SC simulation at rated wind speed.

### 3.2.2 Modeling TMD Position Constraints

One difficulty in the modeling is how to model the stops. Since there is limited space in the nacelle and platforms, stops are necessary to prevent the TMD from exceeding these space requirements. For the NREL 5MW nacelle, the dimensions dictate that the longest stroke for the TMD is $\pm 8m$ in the fore-aft direction, and $\pm 2.5m$ for the side-side TMD. The stops in FAST-SC are modeled as a large spring and damper that come into contact with the mass at a certain set distance from the undeflected TMD spring position. This makes the system highly non-linear. In order to model this in Simulink, a series of $ifelsethen$ statements are used. These statements are inserted in the acceleration equations such that if the mass is hitting the stop, an additional force is applied to the mass and an equal and opposite force is applied to the nacelle or tower. This system gave good agreement with FAST-SC. In Figure 3.9, both the effect of the stops and the non-zero mean thrust loading can be seen.

In this figure, the barge's steady state pitch angle is approximately 3° because of the steady thrust loading. Also, the bottom graph shows the TMD hitting the stop at 8m.

## 3.3 Initial Optimization Attempts

Once the models for the platforms are built and tuned, the next step is to use the models to optimize the TMD parameters. In order to view a graphical representation of the function that was being optimized, a surface response method was employed. This proved useful to visualize how to approach the problem, but did not prove to be a viable optimization method.

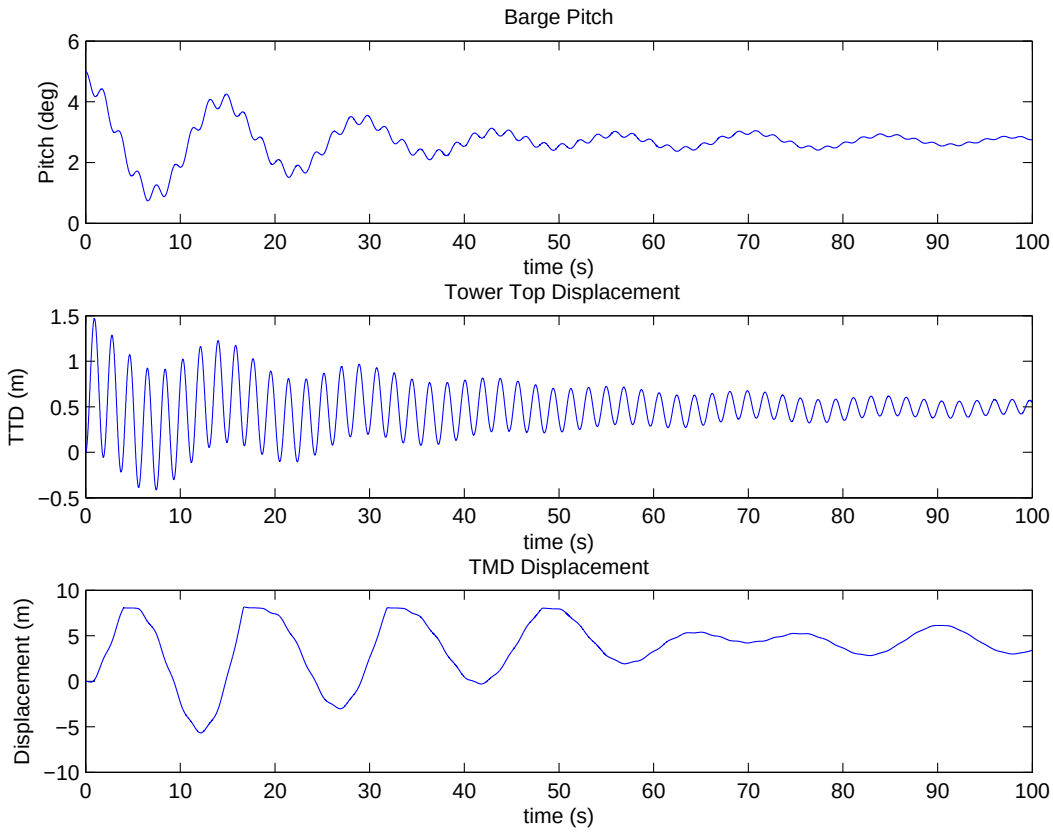


**Figure 3.9.** Figure showing an example of a barge limited DOF model simulation

### 3.3.1 Surface Response Plots

The surface response plots were created by inputing different combinations of spring and damping constants and recording the standard deviation of the tower top displacement, which is an easy to calculate indicator of fatigue. By inputing a range of evenly spaced spring and damping constants, and plotting this array with the standard deviation of tower top displacement on a surface plot, the optimum can be found graphically. Figure 3.10 shows the response of the barge model with a 20,000 kg TMD for various spring and damping constants. For Figure 3.10, no stops were applied, which makes the system linear. There is a very clear optimum in this plot which can be seen as the bottom of the valley on the surface. Without stops, this

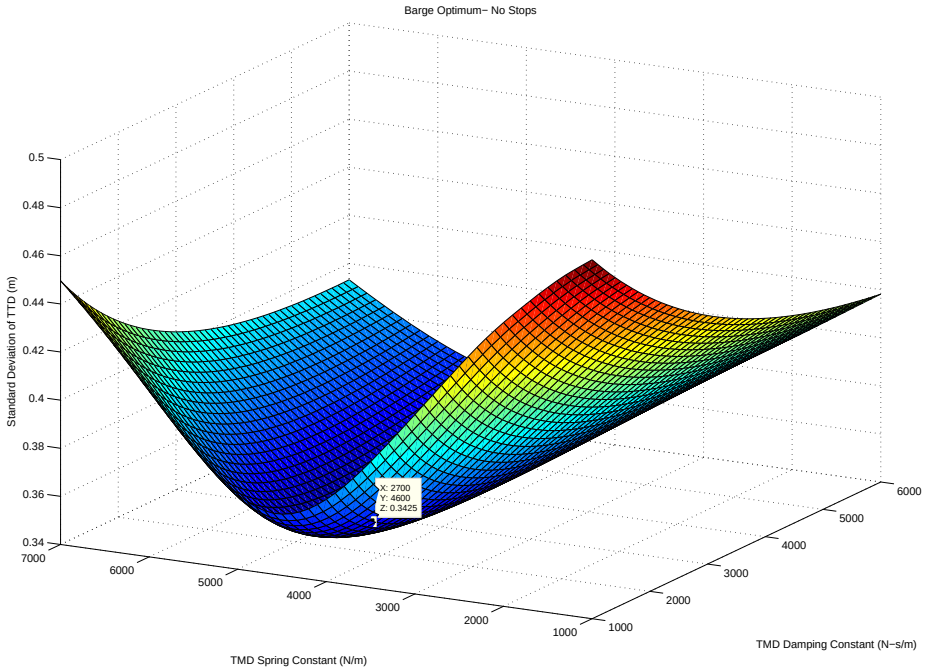


**Figure 3.10.** Surface plot of standard deviation of tower top displacement vs. TMD spring and damping constants for the barge with no stops

curve is very smooth, however, as soon as stops are added, the surface appears as is Figure 3.11.

All parameters and loading conditions are the same for these two plots, only the existence of stops is different. The plot without stops has a clearly defined minimum at $k_{TMD} = 4600N/m, d_{TMD} = 2700N - s/m$. The plot with stops enabled has several local minima, and the global minimum is approximately $k_{TMD} = 2700N/m, d_{TMD} = 4700N - s/m$. (The swap of values is purely coincidental.) It should be noted that for low spring and damping, the mass tends to hit the stops more, but for higher spring and damping, the mass does not hit the stops and the system resembles the linear case. Figure 3.12 shows the difference of Figure 3.10 & 3.11. For high spring and damping constants, the difference in the two plots equals zero, which means the responses are the same with stops or no stops for these cases.

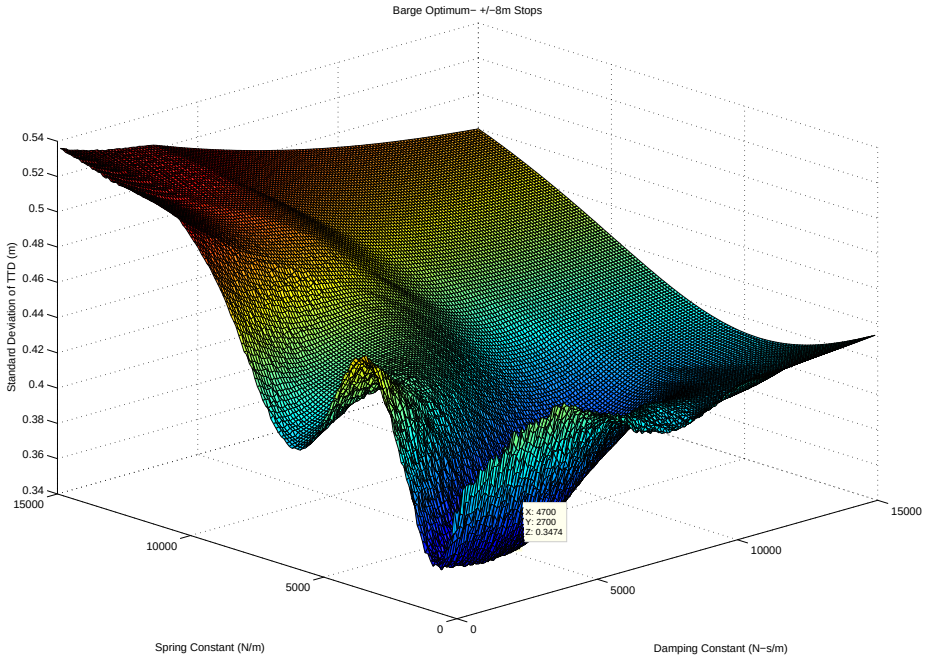


**Figure 3.11.** Surface Plot of standard deviation of tower top displacement vs. TMD spring and damping constants for the barge with stops at $\pm 8m$

Regardless of non-linearity, these surface plots could theoretically be created for all of the models and TMD masses that are desired, and the optimums could be found. However, this approach has a few problems. One is that it is very computationally expensive. Each gridpoint on the surface is a function call, and a full surface may need tens of thousands of gridpoints to be resolved. This could translate to many hours of processor time. The more important reason, however, is that with the non-linearity of the problem, it is hard to be sure that the optimum is captured within the range of spring and damping parameters that are specified. With this in mind, a more elegant optimization algorithm is described next.

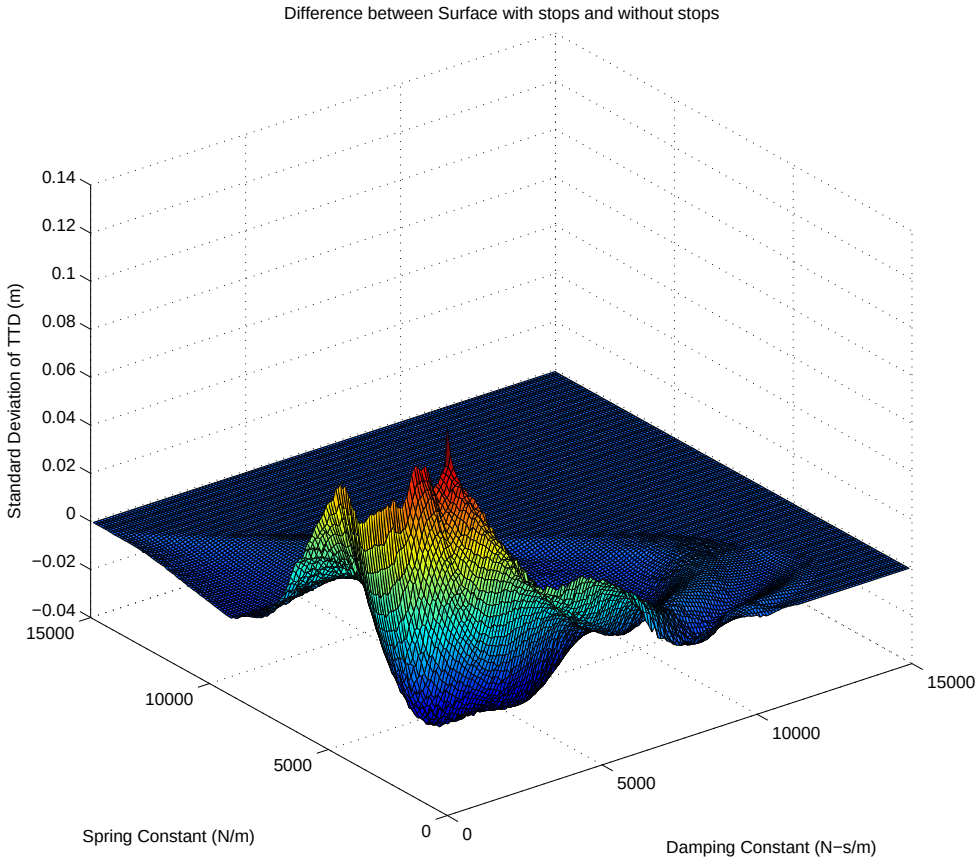


**Figure 3.12.** Surface plot showing the difference between surfaces with stops and no stops.

### 3.3.2 Sequential Quadratic Programming Method

Sequential quadratic programming (SQP) is a common iterative steepest descent method for finding an optimum. Matlab has a built in function that uses this algorithm called fmincon. This algorithm, unfortunately, performs poorly for the cases with stops. Due to the numerous local minima that can be seen in Figure 3.11, the algorithm gets stuck in the closest minima to where it is started. This would be true for all gradient based methods for this problem, so a global optimization technique is needed.

## 3.4 Genetic Algorithm

The global optimization method that was selected for this research is known as a genetic algorithm. It is an evolution inspired algorithm that includes mathematical representations of populations, individual fitness, mutation, and even mating to find an optimum to a problem. The basic theory is that an initial population of designs is generated randomly, and the most fit designs are mated together to produce a new population. This is accomplished by representing designs as binary strings that contain the "genome" of the individual. Even though this sounds far fetched, the math behind it is quite simple. However, there are a few caveats. This algorithm suffers from the same constraint problem as the surface response method; if the optimum is outside the initial range of values chosen, the algorithm will not find it. Compared to the surface response method, however, there is much less computation cost associated with increasing the range of values used, so the search range can be expanded such that there is high confidence in the algorithm finding the global minimum.

### 3.4.1 Implementation

The algorithm used is a modification of the open source SpeedyGA written for Matlab by Keki Burjorjee. This modified code can be seen in AppendixA. The capability of using multiple design variables is introduced so both the spring and damping constants can be specified in one individual. The algorithm starts by picking a population of random binary strings for both the spring and damping constants. These designs are kept in pairs throughout the algorithm. The binary strings are simply binary encodings of the integer value of the corresponding spring or damping constant. The length of these strings put bounds on the variables. For example, if the length is 15, then the maximum value for the parameter is $2^{15} - 1 = 32,767$.

Once the initial population is chosen, the first step is to check fitness values, which are the reciprocal of the standard deviation of tower top displacement. The

reciprocal is used because genetic algorithms find maximum values, not minimums. The checking of fitness values is where the majority of the computational time is taken because the model must be run for each design. Next the algorithm saves the elite and average fitness, and goes on to the scaling, crossover, and mutation steps.

The scaling used is called sigma-scaling, which normalizes the fitnesses by the standard deviation, and removes individuals which are more than one standard deviation below the mean of the population. A roulette wheel uniform crossover is used with a $P_{crossover} = 0.7$. Roulette wheel crossover can be visualized as a weighted roulette wheel. The more fit individuals have a larger slice of the wheel, and thus are more likely to be bred in the crossover. Uniform crossover takes random bits from the strings of both of the parents and swaps them. A mutation probability, $P_{mutation} = 0.01$, per bit is applied, where the algorithm switches 1% of the bits to the opposite of what it was. The mutation step helps to maintain genetic diversity in the population. The process is then repeated.

### 3.4.2 Results of GA

With a population size of 50 individuals, the algorithm converges within approximately 10 generations, as can be seen in Figure3.13.

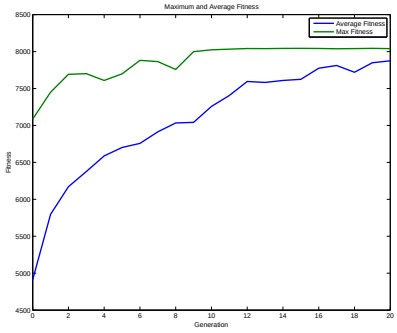


**Figure 3.13.** Convergence of fitness through generations

This amounts to 500 function calls, which takes approximately 30 minutes. This is much more feasible for use than the surface method, which took tens of thousands of function calls. The genetic algorithm is run on all of the platform models and the optimum values can be seen in Table 3.1.

| Platform | TMD Mass (kg) | $k_{tmd}(N/m)$ | $d_{tmd}(N-s/m)$ | TMD Location | Stop Dist |
|---|---|---|---|---|---|
| Barge | 10000 | 1237 | 255 | Nac | $\pm 8m$ |
| Barge | 20000 | 2345 | 1235 | Nac | $\pm 8m$ |
| Barge | 40000 | 5274 | 10183 | Nac | $\pm 8m$ |
| Monopile | 10000 | 28805 | 2800 | Nac | $\pm 8m$ |
| Monopile | 20000 | 54274 | 7414 | Nac | $\pm 8m$ |
| Monopile | 40000 | 98641 | 19690 | Nac | $\pm 8m$ |
| Spar | 10000 | 54151 | 3759 | Nac | $\pm 8m$ |
| Spar | 20000 | 101426 | 10076 | Nac | $\pm 8m$ |
| Spar | 40000 | 183625 | 26747 | Nac | $\pm 8m$ |
| Spar | 100000 | 157 | 57395 | Plat | $\pm 12m$ |
| Spar | 200000 | 440 | 92506 | Plat | $\pm 12m$ |
| Spar | 400000 | 262081 | 131008 | Plat | $\pm 12m$ |
| TLP | 10000 | 12350 | 1300 | Nac | $\pm 8m$ |
| TLP | 20000 | 24500 | 4000 | Nac | $\pm 8m$ |
| TLP | 40000 | 41000 | 8700 | Nac | $\pm 8m$ |
| TLP | 100000 | 56500 | 100 | Plat | $\pm 8m$ |
| TLP | 200000 | 115000 | 200 | Plat | $\pm 8m$ |
| TLP | 400000 | 230000 | 400 | Plat | $\pm 8m$ |

**Table 3.1.** Table showing the results of the genetic algorithm

### 3.4.3 TLP Optimization Method

For the reasons discussed in Section 3.1.4, building a simple mathematical model to represent the tension leg platform is very difficult, and it was decided that using FAST-SC to optimize the TMD is the best option. This is accomplished by a simple parametric study in which a range of spring constants with a constant damping constant is run in a full DOF simulation, and the best spring constant is found for each TMD mass. Next, the spring constants are set to the optimum that was found, and the damping constant is varied. This technique finds a rough optimum for the system, but once again there are windowing issues. Since this is a non-linear system,

there could be an optimum outside of the range of the parameters that were chosen. A more thorough (but time consuming) optimization could use FAST-SC itself as the design function for a global optimization scheme, but for the purposes of this thesis, the parametric study is used.

## 3.5 FAST-SC Simulations

In order to evaluate the effectiveness of the optimal TMD designs, a series of simulations are run to compare baseline cases to the TMD cases. Each case in Table 3.1 was run in FAST-SC for four different wind and wave inputs, as well as a baseline with no TMD and the same wind and wave inputs. A side-side TMD simulation was also run for each case using the same parameters. While the optimal parameters found with the genetic algorithm might not necessarily be optimal for a side-side TMD, it will at least show what effect the side-side TMD has on the platform. Finally, all the cases were run with identical side-side and fore-aft TMDs active. This amounts to 236 separate FAST-SC simulations.

The previous work by Lackner [28] considered a 20,000 kg mass for the TMD in the nacelle of the barge and monopile. This mass was chosen because it is approximately 2% of the total mass of the monopile, which is a mass percentage that is commonly used in civil structures. For the purposes of this thesis, 10,000 kg, 20,000 kg, and 40,000 kg were chosen for TMDs in the nacelle, which equates to approximately 1%, 2%, and 4% of the monopile based offshore wind turbine. For the simulations with the TMD in the platform, 100,000 kg, 200,000 kg, and 400,000 kg are used as masses, as this is approximately 1%, 2%, and 4% of the entire floating structure mass.

When running the simulations for the TLP and spar buoy with the TMD in the platform, it was discovered that simply adding mass to the platform in the form of a TMD has some negative effects. The added mass causes the platform to be positioned lower in the water. This is especially a problem in the case of the TLP, because the

lines become more slack. Also, the natural frequencies of the platform change. For these simulations, the mass and inertia was subtracted from the platform equivalent to the mass and inertia added by the TMD.

### 3.5.1 Results with Monopile with Passive TMD

This section analyzes the results of the simulations of the wind turbine using the monopile foundation and the previously determined optimum TMD constants. Fore-aft and side-side tower fatigue damage are considered, as well as the 95th percentile bending moment that the tower experienced, which can be extrapolated to estimate ultimate loading on the tower. Table 3.2 shows these metrics, as well as the percent improvement over the baseline simulations with no TMD. A negative value for percent improvement indicates an increase in that output compared to the baseline.

| Results of Monopile Simulations | | | | | | | | | | |
|---|---|---|---|---|---|---|---|---|---|---|
| | | Fore-Aft TMD | | | Side-Side TMD | | | Fore-Aft and Side-Side TMDs | | |
| | Baseline | 10,000 kg | 20,000 kg | 40,000 kg | 10,000 kg | 20,000 kg | 40,000 kg | 10,000 kg | 20,000 kg | 40,000 kg |
| Fore-Aft Fatigue Damage (kNm) 10 m/s | 6361 | 5997 | 5968 | 5817 | 6333 | 6328 | 6335 | 5997 | 5857 | 5724 |
| Percent Improvement from Baseline 10 m/s | N/A | 5.7% | 6.2% | 8.5% | 0.4% | 0.5% | 0.4% | 6.1% | 7.9% | 10.0% |
| Fore-Aft Fatigue Damage (kNm) 18 m/s | 10630 | 10100 | 9948 | 9769 | 10641 | 10662 | 10678 | 10100 | 9973 | 9821 |
| Percent Improvement from Baseline 18 m/s | N/A | 5.0% | 6.4% | 8.1% | -0.1% | -0.3% | -0.5% | 4.9% | 6.2% | 7.6% |
| Side-Side Fatigue Damage (kNm) 10 m/s | 2577 | 2625 | 2820 | 2943 | 1182 | 1107 | 1043 | 2625 | 1083 | 1020 |
| Percent Improvement from Baseline 10 m/s | N/A | -1.9% | -9.5% | -14.2% | 54.1% | 57.0% | 59.5% | 55.4% | 58.0% | 60.4% |
| Side-Side Fatigue Damage (kNm) 18 m/s | 7084 | 7101 | 5703 | 6320 | 2989 | 2732 | 2489 | 7101 | 2637 | 2404 |
| Percent Improvement from Baseline 18 m/s | N/A | -0.2% | 19.5% | 10.8% | 57.8% | 61.4% | 64.9% | 58.9% | 62.8% | 66.1% |
| Fore-Aft 95th Percentile Load (kNm) 10 m/s | 43367 | 43060 | 43152 | 43133 | 43368 | 43390 | 43524 | 43060 | 43196 | 43384 |
| Percent Improvement from Baseline 10 m/s | N/A | 0.7% | 0.5% | 0.5% | -0.0% | -0.1% | -0.4% | 0.4% | 0.4% | -0.0% |
| Fore-Aft 95th Percentile Load (kNm) 18 m/s | 32925 | 32836 | 32596 | 32742 | 32958 | 33000 | 33262 | 32836 | 32740 | 32934 |
| Percent Improvement from Baseline 18 m/s | N/A | 0.3% | 1.0% | 0.6% | -0.1% | -0.2% | -1.0% | 0.0% | 0.6% | -0.0% |
| Side-Side 95th Percentile Load (kNm) 10 m/s | 5972 | 5806 | 6070 | 6233 | 5042 | 4970 | 4946 | 5806 | 4984 | 4974 |
| Percent Improvement from Baseline 10 m/s | N/A | 2.8% | -1.6% | -4.4% | 15.6% | 16.8% | 17.2% | 15.8% | 16.5% | 16.7% |
| Side-Side 95th Percentile Load (kNm) 18 m/s | 11626 | 11479 | 10561 | 11095 | 8244 | 8045 | 7897 | 8234 | 8063 | 7976 |
| Percent Improvement from Baseline 18 m/s | N/A | 1.3% | 9.2% | 4.6% | 29.1% | 30.8% | 32.1% | 29.2% | 30.6% | 31.4% |

**Table 3.2.** Table showing the results of the monopile simulations

A number of interesting conclusions can be drawn from these data. As a general rule, as the TMD mass increased, so did the load reduction. However, diminishing returns can be seen in this trend. A plot of the fore-aft tower damage can be seen in Figure 3.14. The four lines represent the 4 different turbulent wind files used. Each line has identical wind and wave loading, the only difference is the TMD mass and parameters. The plots show a sharp drop from the baseline simulation with no TMD to the 10,000 kg TMD, and after that, the mass improves the amount of fatigue

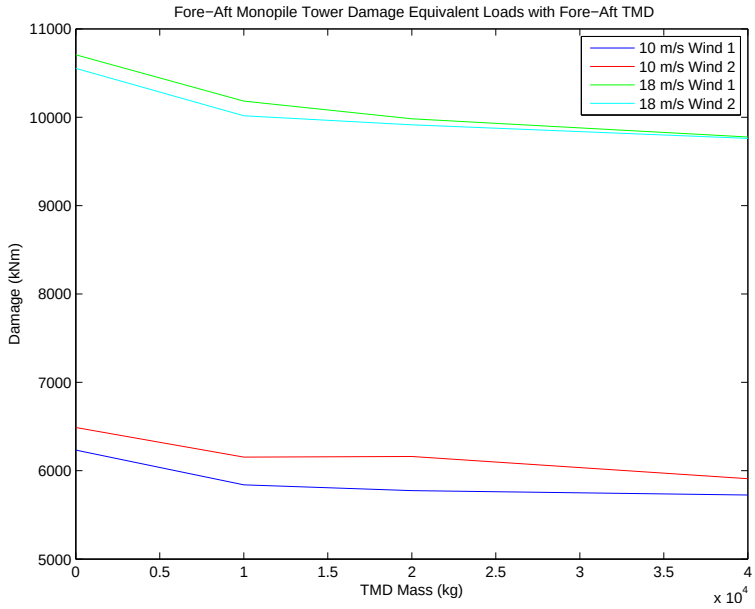


**Figure 3.14.** Plot of fore-aft damage reduction from a fore-aft TMD in the nacelle of the monopile.

damage only slightly. This trend can be seen more sharply in the side-side fatigue graph with a side-side TMD, Figure 3.15. The addition of a 10,000 kg side-side TMD reduces side-side damage by approximately 55%, and the 40,000 kg acheives approximately a 60% reduction.

Although not specifically designed to reduce ultimate loads, the TMD in the monopile reduces the 95th percentile bending moment by approximately 1% in the fore-aft direction, and as much as 32% for side-side loads. This is due to the fact that the TMD reduces the amplitude of the bending moment, which reduces ultimate loads as well as fatigue.

It is also interesting that for both fatigue and ultimate loading, the TMD had a better effect in the side-side direction than the fore-aft. This is most likely because the excitation in the side-side direction is mostly caused by degree of freedom coupling as there is no direct loading in this direction. This results in the side-side bending to have most of its energy in the tower vibrational frequency (see Figure 3.16). In

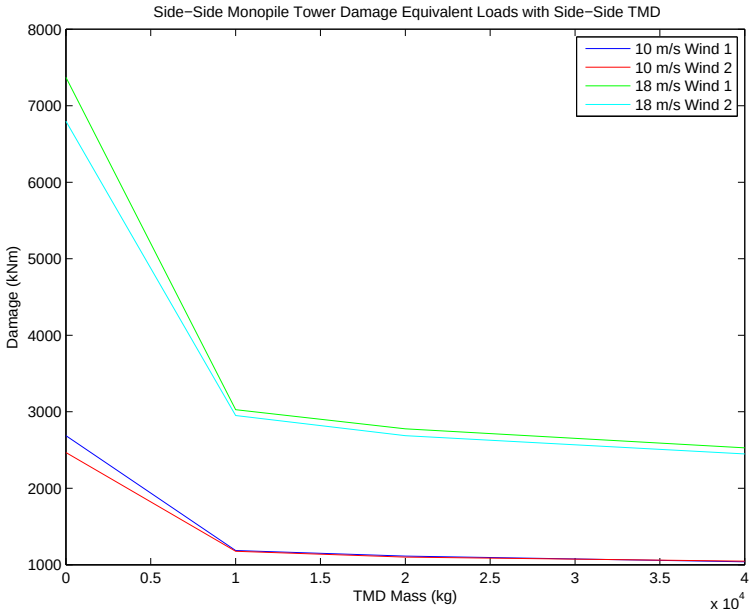


**Figure 3.15.** Plot of side-side damage reduction from a side-side TMD in the nacelle of the monopile.

Figure 3.16 the peak at .28 Hz is the tower vibrational mode. Since the TMD is tuned for this tower vibrational frequency, the TMD is able to damp out much more of the energy in the side-side direction.

In FAST-SC, the wave forcing direction is in the same direction as the wind. With realistic loading conditions, this may not always be the case, as there is some lag between wind and wave forcing. Therefore, this large side-side reduction seen in the FAST-SC simulations may not be a realistic reduction. Further study using misaligned wind and wave forcing is needed to quantify this effect.

### 3.5.2 Barge Results

The wind and wave inputs that were used for the monopile simulation are also used for the barge simulations so that comparisons can be drawn between the two. The table showing both the fatigue damage and the 95th percentile load can be seen in Table 3.3. The trend of diminishing returns is not as apparent for the barge as

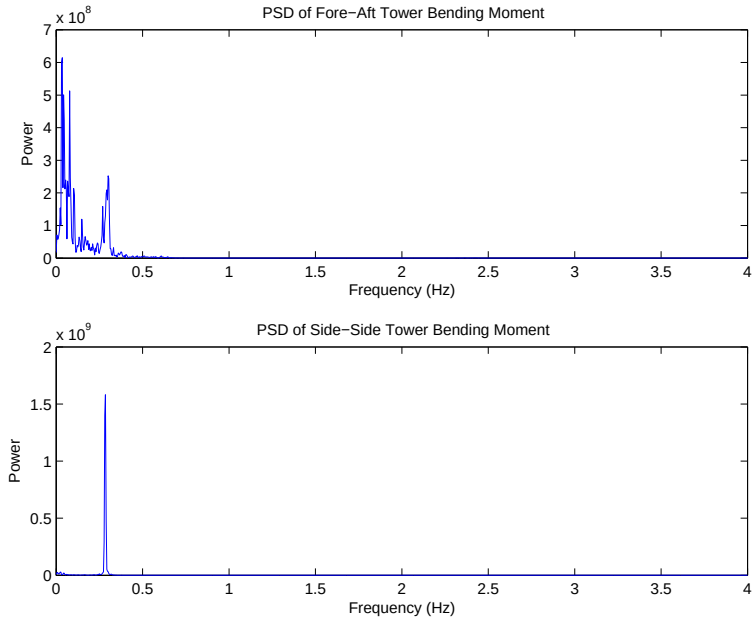


**Figure 3.16.** Plot comparing the power spectrum of fore-aft and side-side bending moments.

the monopile. Figure 3.17 shows the fore-aft tower bending damage with a fore-aft TMD. When compared with Figure 3.14, the slopes of the lines is roughly linear, and does not show the diminishing returns effect seen in the monopile simulations. The ultimate loads for the fore-aft direction, Figure 3.18, were more substantially reduced for the barge than the monopile. Fore-aft 95th percentile loads were reduced by up to 12% from the baseline. Once again, the side-side loads were substantially reduced by the side-side TMD. The reduction in side-side fatigue loads is up to 30% by the TMDs used in these simulations.

### 3.5.3 Spar Results

Two sets of simulations were run for the spar buoy. One uses a nacelle based TMD like the monopile and barge simulations, and the other uses a TMD in the spar itself. A few problems with the spar buoy TMDs were discovered in the course of the research. One is that since the pitching mode of the spar buoy has a low

| Results of Barge Simulations | | | | | | | | | | |
|---|---|---|---|---|---|---|---|---|---|---|
| | | Fore-Aft TMD | | | Side-Side TMD | | | Fore-Aft and Side-Side TMDs | | |
| | Baseline | 10,000 kg | 20,000 kg | 40,000 kg | 10,000 kg | 20,000 kg | 40,000 kg | 10,000 kg | 20,000 kg | 40,000 kg |
| Fore-Aft Fatigue Damage (kNm) 10 m/s | 33684 | 31699 | 29984 | 28424 | 33881 | 34101 | 34647 | 31699 | 30338 | 28879 |
| Percent Improvement from Baseline 10 m/s | N/A | 5.9% | 11.0% | 15.6% | -0.6% | -1.2% | -2.9% | 5.8% | 9.9% | 14.3% |
| Fore-Aft Fatigue Damage (kNm) 18 m/s | 54230 | 52109 | 50354 | 49267 | 54473 | 54739 | 55131 | 52109 | 51689 | 46516 |
| Percent Improvement from Baseline 18 m/s | N/A | 3.9% | 7.1% | 9.2% | -0.4% | -0.9% | -1.7% | 2.8% | 4.7% | 14.2% |
| Side-Side Fatigue Damage (kNm) 10 m/s | 8111 | 8341 | 7869 | 8869 | 8664 | 8236 | 6997 | 8341 | 7408 | 6655 |
| Percent Improvement from Baseline 10 m/s | N/A | -2.8% | 3.0% | -9.3% | -6.8% | -1.5% | 13.7% | -2.5% | 8.7% | 17.9% |
| Side-Side Fatigue Damage (kNm) 18 m/s | 17001 | 15440 | 14728 | 15888 | 15601 | 15231 | 12887 | 15440 | 13349 | 11427 |
| Percent Improvement from Baseline 18 m/s | N/A | 9.2% | 13.4% | 6.5% | 8.2% | 10.4% | 24.2% | 11.8% | 21.5% | 32.8% |
| Fore-Aft 95th Percentile Load (kNm) 10 m/s | 67974 | 66239 | 64078 | 63152 | 71640 | 72178 | 73531 | 66239 | 65403 | 65337 |
| Percent Improvement from Baseline 10 m/s | N/A | 2.6% | 5.7% | 7.1% | -5.4% | -6.2% | -8.2% | 2.0% | 3.8% | 3.9% |
| Fore-Aft 95th Percentile Load (kNm) 18 m/s | 83259 | 80687 | 77836 | 73126 | 84515 | 84869 | 86480 | 80687 | 79398 | 74638 |
| Percent Improvement from Baseline 18 m/s | N/A | 3.1% | 6.5% | 12.2% | -1.5% | -1.9% | -3.9% | 2.3% | 4.6% | 10.4% |
| Side-Side 95th Percentile Load (kNm) 10 m/s | 11049 | 10829 | 10626 | 11702 | 11143 | 10550 | 9353 | 10829 | 9810 | 9156 |
| Percent Improvement from Baseline 10 m/s | N/A | 2.0% | 3.8% | -5.9% | -0.8% | 4.5% | 15.3% | 4.1% | 11.2% | 17.1% |
| Side-Side 95th Percentile Load (kNm) 18 m/s | 21821 | 20991 | 20011 | 21819 | 19487 | 18495 | 16491 | 18834 | 17246 | 15286 |
| Percent Improvement from Baseline 18 m/s | N/A | 3.8% | 8.3% | 0.0% | 10.7% | 15.2% | 24.4% | 13.7% | 21.0% | 29.9% |

**Table 3.3.** Table showing the results of the barge simulations

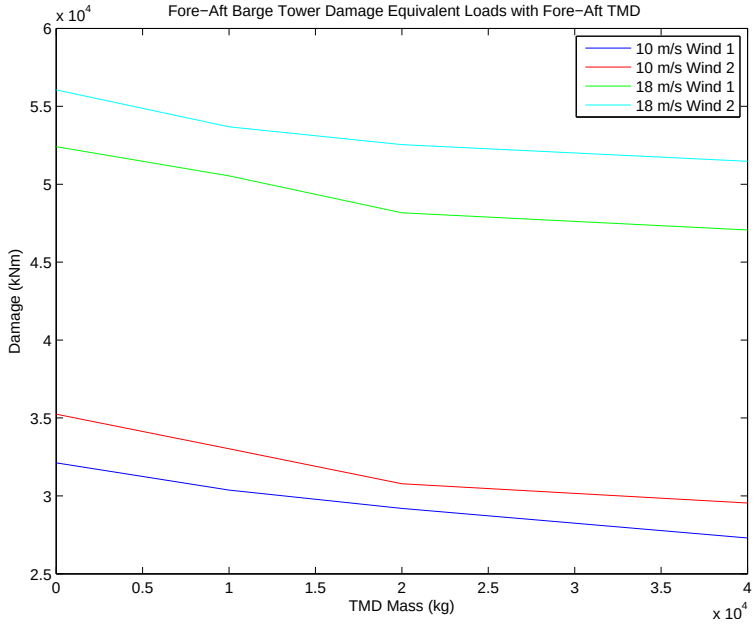


**Figure 3.17.** Plot of fore-aft damage reduction from a fore-aft TMD in the nacelle of the barge turbine.

frequency, requiring a low TMD spring constant. This, in turn, makes the TMD more susceptible to gravity forcing, as there is not a strong enough spring. This would not be a problem with a translational system like a civil structure, but for a pitching system, the gravity forcing on the TMD can not be ignored. This problem is exacerbated by the thrust forcing of the wind. The constant component of the

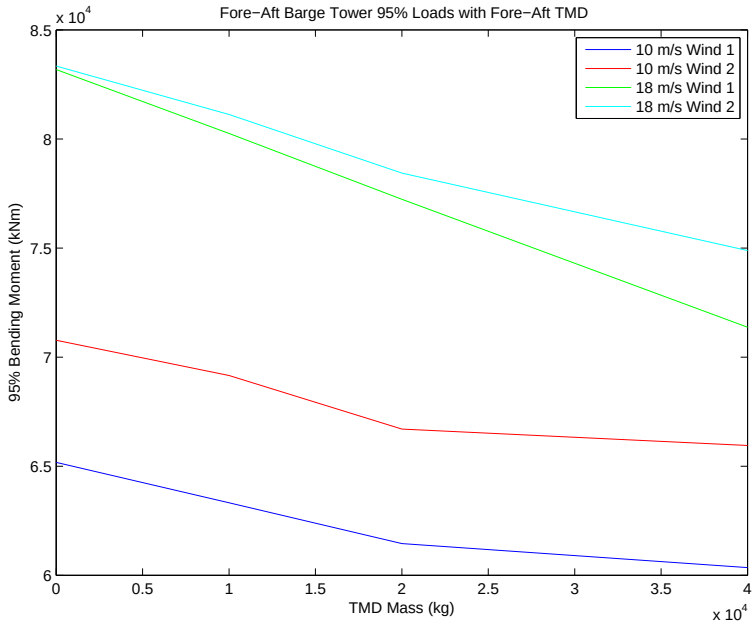


**Figure 3.18.** Plot of fore-aft damage reduction from a fore-aft TMD in the nacelle of the barge turbine.

wind forcing causes the spar to be pitched backward, which in turn forces the TMD against the downwind stop. Figure 3.19 shows the displacement of the TMD during a representative simulation to show the effect of constant thrust.

Another effect of the TMD resting against the stop is that when the TMD is displaced, it creates a gravity moment on the spar buoy. In Equation 3.6, the term $+m_{tmd}g(R_{tmd}\theta_p - x_{tmd})$ encompasses this effect. The TMD mass exerts a vertical gravity force on the spar, and when the TMD is off center, this force turns into a moment, with the moment arm being the distance that the TMD has displaced relative to the spar coordinate system. This term scales with the mass of the TMD and the amount of TMD deflection, so when there is a heavy TMD that is deflected as far as possible, which is the case in the spar, this term becomes a non-negligible destabilizing moment.

The TMD parameters are selected with the gravitational moment integrated since this term is included in the model that the genetic algorithm optimized. For the

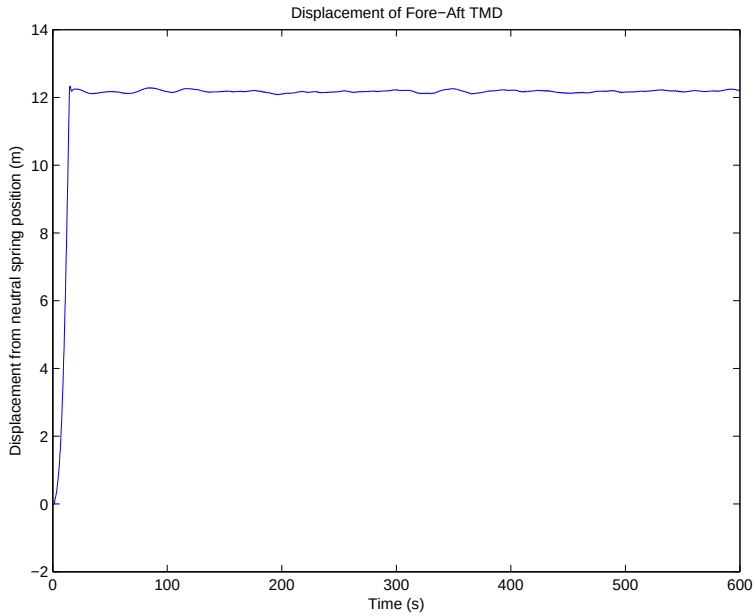


**Figure 3.19.** Plot of fore-aft TMD displacement showing the effect of constant thrust.

400,000 kg mass, this term became too large, and the genetic algorithm chose to maximize the spring and damping constants to force the TMD to stay near the center of the spar, which essentially eliminates the moment arm, and thus, the destabilizing moment. For this reason, the 400,000 kg TMD results are essentially the same as not having a TMD at all, and can be disregarded.

Even with all of these problems, there was improvement in fatigue and ultimate loads in some simulations, which can be seen in Table 3.4. The 18 m/s average wind speed simulations in particular show reductions in tower fatigue and ultimate loads. This is because there is less rotor thrust in these simulations, so the spar pitches less, and the effect of the gravity moment is diminished.

Table 3.5 show the tower bending fatigue of the spar buoy with the TMD moved to the nacelle. This TMD is tuned to the tower first bending mode, which has a much higher frequency than the pitching mode, so the spring constant is higher. This

| Results of Spar Simulations with the TMD in the Platform | | | | | | | | | | |
|---|---|---|---|---|---|---|---|---|---|---|
| | | Fore-Aft TMD | | | Side-Side TMD | | | Fore-Aft and Side-Side TMDs | | |
| | Baseline | 100,000 kg | 200,000 kg | 400,000 kg | 100,000 kg | 200,000 kg | 400,000 kg | 100,000 kg | 200,000 kg | 400,000 kg |
| Fore-Aft Fatigue Damage (kNm) 10 m/s | 15319 | 15217 | 15076 | 15360 | 15263 | 15318 | 15224 | 15217 | 14986 | 15483 |
| Percent Improvement from Baseline 10 m/s | N/A | 0.7% | 1.6% | -0.3% | 0.4% | 0.0% | 0.6% | 1.9% | 2.2% | -1.1% |
| Fore-Aft Fatigue Damage (kNm) 18 m/s | 25048 | 23277 | 22302 | 23586 | 23775 | 24974 | 25024 | 23277 | 23899 | 30169 |
| Percent Improvement from Baseline 18 m/s | N/A | 7.1% | 11.0% | 5.8% | 5.1% | 0.3% | 0.1% | -2.4% | 4.6% | -20.4% |
| Side-Side Fatigue Damage (kNm) 10 m/s | 4683 | 4683 | 4642 | 4381 | 4679 | 5069 | 4735 | 4683 | 4387 | 4206 |
| Percent Improvement from Baseline 10 m/s | N/A | 0.0% | 0.9% | 6.5% | 0.1% | -8.2% | -1.1% | 4.2% | 6.3% | 10.2% |
| Side-Side Fatigue Damage (kNm) 18 m/s | 7043 | 7118 | 6951 | 6156 | 6717 | 8785 | 6807 | 7118 | 7660 | 6672 |
| Percent Improvement from Baseline 18 m/s | N/A | -1.1% | 1.3% | 12.6% | 4.6% | -24.7% | 3.4% | 1.3% | -8.8% | 5.3% |
| Fore-Aft 95th Percentile Load (kNm) 10 m/s | 53595 | 55060 | 56368 | 52718 | 53065 | 52484 | 51670 | 55060 | 51540 | 46554 |
| Percent Improvement from Baseline 10 m/s | N/A | -2.7% | -5.2% | 1.6% | 1.0% | 2.1% | 3.6% | 2.5% | 3.8% | 13.1% |
| Fore-Aft 95th Percentile Load (kNm) 18 m/s | 62515 | 59749 | 59148 | 59850 | 57931 | 62462 | 59536 | 59749 | 59240 | 65129 |
| Percent Improvement from Baseline 18 m/s | N/A | 4.4% | 5.4% | 4.3% | 7.3% | 0.1% | 4.8% | 0.6% | 5.2% | -4.2% |
| Side-Side 95th Percentile Load (kNm) 10 m/s | 7563 | 7437 | 7332 | 7129 | 9970 | 13373 | 7373 | 7437 | 10433 | 6683 |
| Percent Improvement from Baseline 10 m/s | N/A | 1.7% | 3.1% | 5.7% | -31.8% | -76.8% | 2.5% | -18.1% | -37.9% | 11.6% |
| Side-Side 95th Percentile Load (kNm) 18 m/s | 12223 | 12078 | 11718 | 10961 | 15202 | 22487 | 11618 | 15243 | 17213 | 11426 |
| Percent Improvement from Baseline 18 m/s | N/A | 1.2% | 4.1% | 10.3% | -24.4% | -84.0% | 5.0% | -24.7% | -40.8% | 6.5% |

**Table 3.4.** Table showing the results of the spar buoy simulations with the TMD in the platform

reduces the gravitational effect that were seen in the platform based TMD simulations.

| Results of Spar Simulations with the TMD in the Nacelle | | | | | | | | | | |
|---|---|---|---|---|---|---|---|---|---|---|
| | | Fore-Aft TMD | | | Side-Side TMD | | | Fore-Aft and Side-Side TMDs | | |
| | Baseline | 10,000 kg | 20,000 kg | 40,000 kg | 10,000 kg | 20,000 kg | 40,000 kg | 10,000 kg | 20,000 kg | 40,000 kg |
| Fore-Aft Fatigue Damage (kNm) 10 m/s | 15319 | 15026 | 14647 | 14034 | 15261 | 14985 | 14449 | 15026 | 14447 | 13670 |
| Percent Improvement from Baseline 10 m/s | N/A | 1.9% | 4.4% | 8.4% | 0.4% | 2.2% | 5.7% | 2.2% | 5.7% | 10.8% |
| Fore-Aft Fatigue Damage (kNm) 18 m/s | 25048 | 25290 | 24406 | 25859 | 24798 | 24758 | 24141 | 25290 | 24939 | 28254 |
| Percent Improvement from Baseline 18 m/s | N/A | -1.0% | 2.6% | -3.2% | 1.0% | 1.2% | 3.6% | 4.0% | 0.4% | -12.8% |
| Side-Side Fatigue Damage (kNm) 10 m/s | 4683 | 3946 | 3662 | 3055 | 4415 | 3893 | 3387 | 3946 | 3392 | 2902 |
| Percent Improvement from Baseline 10 m/s | N/A | 15.7% | 21.8% | 34.8% | 5.7% | 16.9% | 27.7% | 15.1% | 27.6% | 38.0% |
| Side-Side Fatigue Damage (kNm) 18 m/s | 7043 | 5809 | 5654 | 6011 | 6367 | 6124 | 5441 | 5809 | 5057 | 5136 |
| Percent Improvement from Baseline 18 m/s | N/A | 17.5% | 19.7% | 14.6% | 9.6% | 13.0% | 22.7% | 17.3% | 28.2% | 27.1% |
| Fore-Aft 95th Percentile Load (kNm) 10 m/s | 53595 | 54334 | 55042 | 56255 | 54644 | 55686 | 58110 | 54334 | 57192 | 61412 |
| Percent Improvement from Baseline 10 m/s | N/A | -1.4% | -2.7% | -5.0% | -2.0% | -3.9% | -8.4% | -3.5% | -6.7% | -14.6% |
| Fore-Aft 95th Percentile Load (kNm) 18 m/s | 62515 | 63727 | 62086 | 65036 | 63042 | 60855 | 63219 | 63727 | 63439 | 74262 |
| Percent Improvement from Baseline 18 m/s | N/A | -1.9% | 0.7% | -4.0% | -0.8% | 2.7% | -1.1% | 1.9% | -1.5% | -18.8% |
| Side-Side 95th Percentile Load (kNm) 10 m/s | 7563 | 7191 | 7118 | 6953 | 7366 | 7365 | 7545 | 7191 | 7359 | 7781 |
| Percent Improvement from Baseline 10 m/s | N/A | 4.9% | 5.9% | 8.1% | 2.6% | 2.6% | 0.2% | 2.9% | 2.7% | -2.9% |
| Side-Side 95th Percentile Load (kNm) 18 m/s | 12223 | 12054 | 11981 | 12511 | 12128 | 12681 | 12278 | 12201 | 11710 | 14007 |
| Percent Improvement from Baseline 18 m/s | N/A | 1.4% | 2.0% | -2.4% | 0.8% | -3.7% | -0.4% | 0.2% | 4.2% | -14.6% |

**Table 3.5.** Table showing the results of the spar buoy simulations with the TMD in the Nacelle

These results show good fatigue reduction in both the fore-aft and side-side directions, but little ultimate load reduction. In most simulations, the ultimate loads were actually increased.

### 3.5.4 TLP Results

As discussed in Section 3.1.4, the TMD tuned to the surge degree of freedom did reduce platform surge, but this had little effect on mooring line fatigue or tower

bending. Therefore, a TMD tuned to the faster pitching mode was developed. Like the spar buoy, this platform is compatible with both a nacelle based and platform based TMD. Table 3.6 shows the tower loading results from the simulations with the TMD in the nacelle.

| Results of TLP Simulations with the TMD in the Nacelle | | | | | | | | | | |
|---|---|---|---|---|---|---|---|---|---|---|
| | | Fore-Aft TMD | | | Side-Side TMD | | | Fore-Aft and Side-Side TMDs | | |
| | Baseline | 10,000 kg | 20,000 kg | 40,000 kg | 10,000 kg | 20,000 kg | 40,000 kg | 10,000 kg | 20,000 kg | 40,000 kg |
| Fore-Aft Fatigue Damage (kNm) 10 m/s | 13926 | 13425 | 13110 | 12837 | 14159 | 14515 | 15210 | 13425 | 13271 | 13411 |
| Percent Improvement from Baseline 10 m/s | N/A | 3.6% | 5.9% | 7.8% | -1.7% | -4.2% | -9.2% | 3.8% | 4.7% | 3.7% |
| Fore-Aft Fatigue Damage (kNm) 18 m/s | 23370 | 22923 | 22674 | 22566 | 23793 | 24278 | 25311 | 22923 | 23261 | 23769 |
| Percent Improvement from Baseline 18 m/s | N/A | 1.9% | 3.0% | 3.4% | -1.8% | -3.9% | -8.3% | 1.3% | 0.5% | -1.7% |
| Side-Side Fatigue Damage (kNm) 10 m/s | 3392 | 3481 | 3491 | 3398 | 3118 | 2903 | 2804 | 3481 | 2836 | 2675 |
| Percent Improvement from Baseline 10 m/s | N/A | -2.6% | -2.9% | -0.2% | 8.1% | 14.4% | 17.3% | 8.9% | 16.4% | 21.1% |
| Side-Side Fatigue Damage (kNm) 18 m/s | 7394 | 7384 | 7445 | 7958 | 7020 | 6759 | 6626 | 7384 | 6356 | 6110 |
| Percent Improvement from Baseline 18 m/s | N/A | 0.1% | -0.7% | -7.6% | 5.1% | 8.6% | 10.4% | 8.3% | 14.0% | 17.4% |
| Fore-Aft 95th Percentile Load (kNm) 10 m/s | 68827 | 68606 | 68588 | 68739 | 69073 | 69425 | 70173 | 68606 | 68922 | 69392 |
| Percent Improvement from Baseline 10 m/s | N/A | 0.3% | 0.3% | 0.1% | -0.4% | -0.9% | -2.0% | 0.1% | -0.1% | -0.8% |
| Fore-Aft 95th Percentile Load (kNm) 18 m/s | 55182 | 55032 | 54940 | 54964 | 55639 | 55982 | 57128 | 55032 | 55434 | 56282 |
| Percent Improvement from Baseline 18 m/s | N/A | 0.3% | 0.4% | 0.4% | -0.8% | -1.5% | -3.5% | 0.3% | -0.5% | -2.0% |
| Side-Side 95th Percentile Load (kNm) 10 m/s | 6592 | 6631 | 6703 | 6682 | 6381 | 6231 | 6181 | 6631 | 6185 | 6139 |
| Percent Improvement from Baseline 10 m/s | N/A | -0.6% | -1.7% | -1.4% | 3.2% | 5.5% | 6.2% | 3.4% | 6.2% | 6.9% |
| Side-Side 95th Percentile Load (kNm) 18 m/s | 11938 | 11892 | 12150 | 12865 | 11746 | 11486 | 11244 | 11524 | 11166 | 11012 |
| Percent Improvement from Baseline 18 m/s | N/A | 0.4% | -1.8% | -7.8% | 1.6% | 3.8% | 5.8% | 3.5% | 6.5% | 7.8% |

**Table 3.6.** Table showing the results of the TLP simulations with the TMD in the nacelle

Fore-aft bending is reduced by up to 8%, and side-side bending up to 20%. For the TLP, the side-side TMD negatively impacts the fore-aft bending, and the fore-aft TMD causes more damage to the side-side tower degree of freedom. This effect was seen for the other platforms, but not to the extent that it occurs for the TLP.

In addition to tower loads, this TMD is also targeted towards reducing mooring line loading. Table 3.7 shows the fatigue damage and 95th percentile tensile load on the mooring line with the highest loading. Mooring line fatigue damage is reduced

| Results of TLP Simulations with the TMD in the Nacelle | | | | | | | | | | |
|---|---|---|---|---|---|---|---|---|---|---|
| | | Fore-Aft TMD | | | Side-Side TMD | | | Fore-Aft and Side-Side TMDs | | |
| | Baseline | 10,000 kg | 20,000 kg | 40,000 kg | 10,000 kg | 20,000 kg | 40,000 kg | 10,000 kg | 20,000 kg | 40,000 kg |
| Line Fatigue Damage (kN) 10 m/s | 372 | 364 | 357 | 347 | 388 | 388 | 389 | 364 | 363 | 350 |
| Percent Improvement from Baseline 10 m/s | N/A | 2.2% | 4.0% | 6.8% | -4.3% | -4.3% | -4.6% | -0.5% | 2.3% | 5.9% |
| Line Fatigue Damage (kN) 18 m/s | 599 | 588 | 578 | 563 | 601 | 603 | 609 | 588 | 577 | 563 |
| Percent Improvement from Baseline 18 m/s | N/A | 1.9% | 3.4% | 6.1% | -0.4% | -0.7% | -1.7% | 2.2% | 3.6% | 6.1% |
| Line 95th Percentile Load (kN) 10 m/s | 4989 | 4983 | 4977 | 4975 | 5096 | 5083 | 5066 | 4983 | 5050 | 4997 |
| Percent Improvement from Baseline 10 m/s | N/A | 0.1% | 0.2% | 0.3% | -2.2% | -1.9% | -1.5% | -1.8% | -1.2% | -0.2% |
| Line 95th Percentile Load (kN) 18 m/s | 4916 | 4912 | 4903 | 4889 | 5019 | 5009 | 4988 | 4912 | 4977 | 4914 |
| Percent Improvement from Baseline 18 m/s | N/A | 0.1% | 0.3% | 0.5% | -2.1% | -1.9% | -1.5% | -1.8% | -1.2% | 0.0% |

**Table 3.7.** Table showing the results of the TLP simulations with the TMD in the nacelle

by up to 7% with a fore-aft TMD, but the ultimate load is virtually unchanged.

Since the platform in the TLP has a 45 m draft, there is both space and a suitable moment arm to encourage trying a TMD in the platform. The 45 m moment arm is less than the nacelle's 90 m distance to the water level, but the platform based TMD can use a larger mass. Table 3.8 shows the effect of the platform-based TMD on tower loading. This configuration performed poorly for reducing tower bending. This is most likely because the TMD cannot directly apply forces to the tower like the TMD in the nacelle can.

| Results of TLP Simulations with the TMD in the Platform | | | | | | | | | | |
|---|---|---|---|---|---|---|---|---|---|---|
| | | Fore-Aft TMD | | | Side-Side TMD | | | Fore-Aft and Side-Side TMDs | | |
| | Baseline | 100,000 kg | 20,000 kg | 400,000 kg | 100,000 kg | 200,000 kg | 400,000 kg | 100,000 kg | 200,000 kg | 400,000 kg |
| Fore-Aft Fatigue Damage (kNm) 10 m/s | 13926 | 13883 | 13797 | 13822 | 18083 | 24167 | 26605 | 13883 | 23907 | 26099 |
| Percent Improvement from Baseline 10 m/s | N/A | 0.3% | 0.9% | 0.7% | -29.9% | -73.5% | -91.1% | -29.2% | -71.7% | -87.4% |
| Fore-Aft Fatigue Damage (kNm) 18 m/s | 23370 | 23267 | 23293 | 23483 | 29095 | 35288 | 41007 | 23267 | 35010 | 41421 |
| Percent Improvement from Baseline 18 m/s | N/A | 0.4% | 0.3% | -0.5% | -24.5% | -51.0% | -75.5% | -23.9% | -49.8% | -77.2% |
| Side-Side Fatigue Damage (kNm) 10 m/s | 3392 | 3414 | 3467 | 3495 | 4444 | 4773 | 6460 | 3414 | 4780 | 6449 |
| Percent Improvement from Baseline 10 m/s | N/A | -0.6% | -2.2% | -3.0% | -31.0% | -40.7% | -90.4% | -30.9% | -40.9% | -90.1% |
| Side-Side Fatigue Damage (kNm) 18 m/s | 7394 | 7371 | 7252 | 7165 | 9387 | 10953 | 11308 | 7371 | 10990 | 11245 |
| Percent Improvement from Baseline 18 m/s | N/A | 0.3% | 1.9% | 3.1% | -27.0% | -48.1% | -52.9% | -26.8% | -48.6% | -52.1% |
| Fore-Aft 95th Percentile Load (kNm) 10 m/s | 68827 | 68773 | 68800 | 68694 | 72656 | 78503 | 84382 | 68773 | 78420 | 83953 |
| Percent Improvement from Baseline 10 m/s | N/A | 0.1% | 0.0% | 0.2% | -5.6% | -14.1% | -22.6% | -5.6% | -13.9% | -22.0% |
| Fore-Aft 95th Percentile Load (kNm) 18 m/s | 55182 | 55131 | 54916 | 55265 | 60421 | 67106 | 75552 | 55131 | 66838 | 76205 |
| Percent Improvement from Baseline 18 m/s | N/A | 0.1% | 0.5% | -0.2% | -9.5% | -21.6% | -36.9% | -9.2% | -21.1% | -38.1% |
| Side-Side 95th Percentile Load (kNm) 10 m/s | 6592 | 6570 | 6602 | 6683 | 7838 | 8429 | 11027 | 6570 | 8454 | 10996 |
| Percent Improvement from Baseline 10 m/s | N/A | 0.3% | -0.2% | -1.4% | -18.9% | -27.9% | -67.3% | -19.0% | -28.2% | -66.8% |
| Side-Side 95th Percentile Load (kNm) 18 m/s | 11938 | 11949 | 11892 | 11846 | 14113 | 16492 | 17147 | 14116 | 16530 | 17021 |
| Percent Improvement from Baseline 18 m/s | N/A | -0.1% | 0.4% | 0.8% | -18.2% | -38.1% | -43.6% | -18.2% | -38.5% | -42.6% |

**Table 3.8.** Table showing the results of the TLP simulations with the TMD in the platform

Table 3.9 shows the effect of the TMD in the platform on mooring line loading. The TMD in the nacelle had better performance, with the platform based TMD only achieving a 1.3% reduction. This is due to the shorter moment arm combined with the gravitational moment effect described in Section 3.5.3

### 3.5.5 Sensitivity Study

In order to investigate the robustness of the optimum found by the genetic algorithm, a sensitivity study was conducted to quantify the change in fatigue reduction with a change in the TMD parameters. The barge platform was used for this study. FAST-SC was run for with a TMD spring constant that is 10% higher and 10% lower

| Results of TLP Simulations with the TMD in the Platform | | | | | | | | | | |
|---|---|---|---|---|---|---|---|---|---|---|
| | | Fore-Aft TMD | | | Side-Side TMD | | | Fore-Aft and Side-Side TMDs | | |
| | Baseline | 100,000 kg | 200,000 kg | 400,000 kg | 100,000 kg | 200,000 kg | 400,000 kg | 100,000 kg | 200,000 kg | 400,000 kg |
| Fore-Aft Fatigue Damage (kNm) 10 m/s | 372 | 370 | 368 | 367 | 398 | 433 | 400 | 370 | 427 | 390 |
| Percent Improvement from Baseline 10 m/s | N/A | 0.5% | 0.9% | 1.3% | -7.1% | -16.4% | -7.6% | -6.5% | -14.9% | -4.9% |
| Fore-Aft Fatigue Damage (kNm) 18 m/s | 599 | 595 | 594 | 592 | 629 | 636 | 598 | 595 | 630 | 598 |
| Percent Improvement from Baseline 18 m/s | N/A | 0.6% | 0.9% | 1.2% | -5.0% | -6.3% | 0.1% | -4.3% | -5.1% | 0.1% |
| Fore-Aft 95th Percentile Load (kNm) 10 m/s | 4989 | 4988 | 4985 | 4983 | 5015 | 5062 | 5054 | 4988 | 5060 | 5052 |
| Percent Improvement from Baseline 10 m/s | N/A | 0.0% | 0.1% | 0.1% | -0.5% | -1.5% | -1.3% | -0.5% | -1.4% | -1.3% |
| Fore-Aft 95th Percentile Load (kNm) 18 m/s | 4916 | 4913 | 4907 | 4901 | 4933 | 4969 | 4928 | 4913 | 4955 | 4930 |
| Percent Improvement from Baseline 18 m/s | N/A | 0.1% | 0.2% | 0.3% | -0.4% | -1.1% | -0.2% | -0.3% | -0.8% | -0.3% |

**Table 3.9.** Table showing the results of the TLP simulations with the TMD in the platform

than the optimum found with the genetic algorithm, and a TMD damping constant that is 10% higher and lower than the optimum. The change in fatigue damage from the optimum for these cases is shown in Table 3.10.

| | Percentage Increase in Fore-Aft Tower Fatigue Damage from Optimum | | | |
|---|---|---|---|---|
| TMD Mass (kg) | +10% Damping Constant | -10% Damping Constant | +10% Spring Constant | -10% Spring Constant |
| 10,000 | 0.91 | 0.55 | 1.03 | -0.06 |
| 20,000 | 0.38 | 0.63 | 1.52 | -1.16 |
| 40,000 | 0.17 | 0.77 | 1.24 | -0.32 |

**Table 3.10.** Table showing the results sensitivity study using the barge floating platform

In Table 3.10, it can be seen that in general, a 10% change in TMD parameters results in a much smaller change in tower fatigue damage, which means that the system is robust to inconsistancies in the TMD parameters. Changing the spring constant seems to have more effect on the tower fatigue than changing the damping constant, with changes of over 1%. This is most likely due to the fact that changing the spring constant changes the TMD frequency tuning. One other important conclusion of this sensitivity study is that the spring constant is mistuned for the barge, because with a 10% reduction in TMD spring constant, there is a further reduction in tower fatigue damage. However, this additional reduction is small, so the optimum found by the genetic algorithm is close to the true optimum.

# CHAPTER 4

# CONTROL STRUCTURE INTERACTION

The goal of the research on control-structure interaction (CSI) is to build on the previous study that developed an active controller for the barge by adding actuator dynamics, and investigating the effects. First, a limited degree of freedom model is built to enable an analytical frequency domain analysis of the system. Using the insight gained from the frequency domain analysis, a full DOF FAST-SC simulation is conducted to test the original controllers with the new motor model. Finally, the original analysis of the active controller is compared with the new data from the updated actuator model simulations.

## 4.1 Limited Degree of Freedom Model

A limited degree of freedom model was needed for the barge in the CSI research. The model that was developed in Section 3.1.2 is used for this research with a few modifications. In order to model the actuator, a force term was added to the TMD equation as well as the tower equation. The modified equations can be seen in Equations 4.1-4.3.

$$I_p\ddot{\theta}_p = -d_p\dot{\theta}_p - k_p\theta_p - m_pgR_p\theta_p + k_t(\theta_t - \theta_p) + d_t(\dot{\theta}_t - \dot{\theta}_p) \tag{4.1}$$

$$\begin{aligned} I_t\ddot{\theta}_t = {} & m_tgR_t\theta_t - k_t(\theta_t - \theta_p) - d_t(\dot{\theta}_t - \dot{\theta}_p) - k_{TMD}R_{TMD}(R_{TMD}\theta_t - x_{TMD}) \\ & - d_{TMD}R_{TMD}(R_{TMD}\dot{\theta}_t - \dot{x}_{TMD}) \\ & - m_{TMD}g(R_{TMD}\theta_t - x_{TMD}) - R_{TMD}f_a \end{aligned} \tag{4.2}$$

$$\begin{aligned} m_{TMD}\ddot{x}_{TMD} = {} & k_{TMD}(R_{TMD}\theta_t - x_{TMD}) + d_{TMD}(R_{TMD}\dot{\theta}_t - \dot{x}_{TMD}) \\ & + m_{TMD}g\theta_t + f_a \end{aligned} \tag{4.3}$$

These equations are identical to Equations 3.3-3.5 except $f_a$ is added to represent actuator force. The equations are tuned in the same way that is outlined in Section 3.2.

## 4.2 Frequency Domain Analysis

In the literature on control structure interaction, frequency analyses are used to identify CSI, so this method is applied to the barge model. The frequency analysis could have been applied to a FAST-SC model as well, but with a simple linear model, the transfer functions can be solved analytically, which allows for greater insight into the problem.

Using the limited degree of freedom model identified in Section 4.1, a frequency domain analysis was preformed in order to investigate the effects of actuator force on the response of the structure. Equations (4.4)-(4.6) are the Laplace transforms of the equations of motion, Equations 4.1-4.3.

$$I_b\, s^2\, \Theta_b = -d_b\, s\, \Theta_b - k_b\, \Theta_b - m_b\, g\, R_b\, \Theta_b + k_t\, (\Theta_t - \Theta_b) + d_t\, s\, (\Theta_t - \Theta_b) \tag{4.4}$$

$$\begin{aligned} I_t\, s^2\, \Theta_t = {} & m_t\, g\, R_t\, \Theta_t - k_t\, (\Theta_t - \Theta_b) - d_t\, s\, (\Theta_t - \Theta_b) \\ & - k_{TMD}\, R_{TMD}\, (R_{TMD}\, \Theta_t - X_{TMD}) \\ & - d_{TMD}\, R_{TMD}\, s\, (R_{TMD}, \Theta_t - X_{TMD}) \\ & - m_{TMD}\, g\, (R_{TMD}\, \Theta_t - X_{TMD}) - R_{TMD}\, F_a \end{aligned} \tag{4.5}$$

$$\begin{aligned} m_{TMD}\, s^2\, X_{TMD} = {} & k_{TMD}\, (R_{TMD}\, \Theta_t - X_{TMD}) + d_{TMD}\, s\, (R_{TMD}\, \Theta_t - X_{TMD}) \\ & + m_{TMD}\, g\, \Theta_t + F_a \end{aligned} \tag{4.6}$$

In the HMD configurations, an electric motor is needed to generate the control force. The motor is modeled as a permanent magnet DC motor, due to the linear characteristic equation (Equation 4.7), availability of motor constants, and clear control-structure feedback path [4]. While actual large scale applications in civil structures often use AC servomotors, CSI is a consideration for any actuator, and the DC motor allows for a concise analysis [8]. Future work could analyze the effects of different actuators on CSI.

$$\dot{T_m} = -\frac{R_a}{L_a}\, T_m - \frac{K_b\, K_i\, K_g}{L_a\, r_m}\, \dot{x}_{TMD} + \frac{K_i}{L_a}\, V_t \tag{4.7}$$

$R_a$ is the armature resistance, $L_a$ is the armature inductance, $T_m$ is the motor torque, $\dot{x}_{TMD}$ is the speed of the HMD mass, $V_t$ is the applied voltage, $K_b$ is the back electromotive force (EMF) constant, $K_i$ is the motor torque constant, and $K_g$ and $r_m$ are the gear ratio and the lead of the ball screw, which converts the motor rotation into linear motion. The values of these constants used in the analysis can be found in Table 4.1 [25]. This motor was chosen from a handbook on direct current motors based on the power requirements that were estimated in the previous work on the active controller.

| | |
|---|---|
| $K_i$ | 1.2 Nm/A |
| $K_b$ | 1.27 V/s |
| $K_g$ | 1 |
| $R_a$ | .0099 $\Omega$ |
| $r_m$ | .15 m |
| $L_a$ | .00073 H |

**Table 4.1.** Motor Constants for 505 Frame [25]

The force applied to the mass is defined in Equation (4.8).

$$f_a = \frac{T_m K_g}{r_m} \tag{4.8}$$

An equation for force and its transform, Equation (4.9 and 4.10), can be made by combining Equation (4.7) and Equation (4.8).

$$\dot{f}_a = -\frac{R_a}{L_a} f_a - \frac{K_b K_i K_g^2}{L_a r_m^2} \dot{x}_{TMD} + \frac{K_i K_g}{L_a r_m} v_t \tag{4.9}$$

$$s F_a = -\frac{R_a}{L_a} F_a - \frac{K_b K_i K_g^2}{L_a r_m^2} s X_{TMD} + \frac{K_i K_g}{L_a r_m} V_t \tag{4.10}$$

Combining Equation (4.10) and Equations (4.4)-(4.6) leads to the system transfer functions. These functions include $G_{FV}$, the transfer function from voltage to motor force, $G_{\theta F}$, the transfer function from motor force to tower acceleration, and $G_{\theta V}$ the transfer function from voltage to tower acceleration. Tower acceleration is used because it is positively correlated to tower load. See Figure 4.1 for a block diagram of the system. These transfer functions are very complex, with over a thousand terms, however, using MatLab's symbolic toolbox analytical equations can be obtained.

The Bode plot of the structure transfer function, $G_{\theta F}$, can be seen in Figure 4.2, and shows the poles of the structure at .574 rad/s and 3.4 rad/s, which correspond to the barge and tower natural frequencies, respectively. The Bode plot of $G_{FV}$, also in

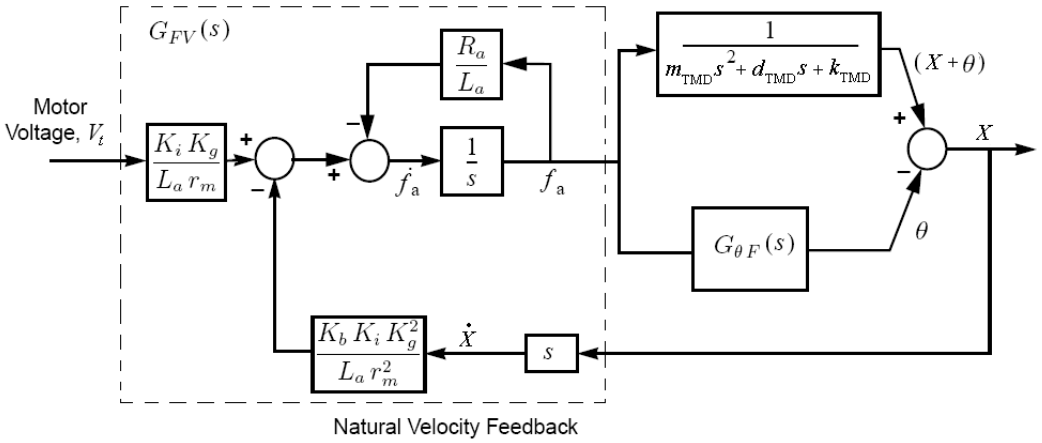


**Figure 4.1.** Block diagram showing feedback path [4]

Figure 4.2, shows the effects of CSI clearly. At the two structure poles, the actuator has zeros (refer to Figure 4.3 for a clearer depiction of these zeros). Because of the zeros, the actuator is least effective at the natural frequencies of the structure. The drop in force magnitude at higher frequencies is due to the inductance of the motor, but the system is seldom operated at these frequencies, so the effect of inductance is negligible. The combined Bode plot, $G_{\theta V}$, is simply the product of the structure transfer function and the motor transfer function, which is the middle line in Figure 4.2.

### 4.2.1 Effect of Gear Ratio on CSI

Changing the motor gear ratio, which can be seen as $K_g/r_m$ in Equation (4.10), can have a large effect on CSI. This term has units of $rad/m$, and is the number of radians that the motor needs to turn to move the mass one meter. The $X$ term in Equation (4.10) has the gear ratio squared in the coeffecient, and the voltage term has the gear ratio to the first power. Since control-structure interaction is caused by the effect of the $X$ term, by reducing the gear ratio, one can reduce the magnitude of the $X$ coefficient in relation to the voltage coefficient, and reduce the effect of CSI. This

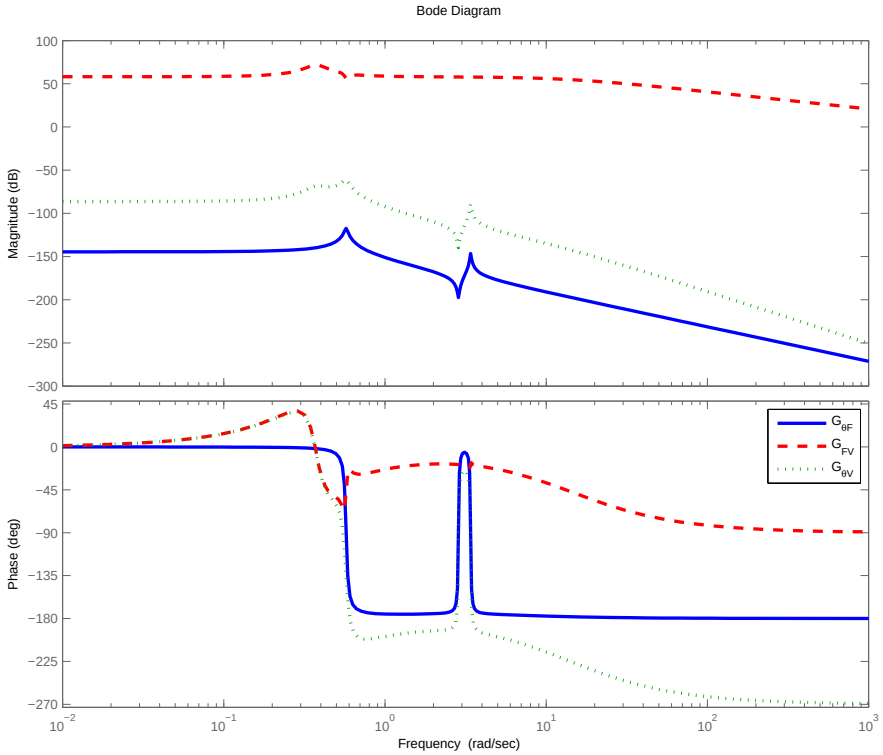


**Figure 4.2.** Figure showing the three transfer functions

phenomenon can be seen in Figure 4.3, which compares the motor transfer function of different gear ratios. These gear ratios were selected in order to give a reasonable range of motor speeds for the motor size that is used.

As the gear ratio is reduced, the transfer function starts to resemble a low-pass filter due to the inductance. Within the frequency of operation, the magnitude of the force is flat, so the impact of CSI is diminished. This effect has not been shown in previous investigations of CSI, and provides insight into how to design the mechanical components of the actuator to minimize unwanted CSI effects.

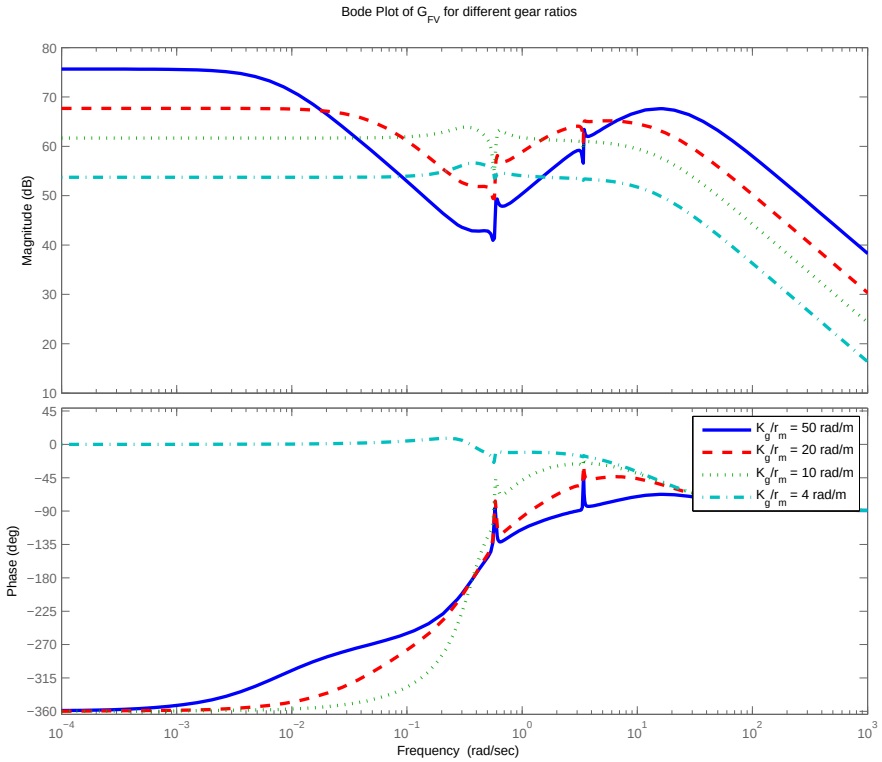


**Figure 4.3.** Bode Plot of motors with different gear ratios

## 4.3 FAST-SC Simulation of Active Control of Wind Turbines with CSI

Simulations are now performed in the time domain using FAST-SC, a state of the art aero-elastic design code described in Section 3.1. These simulations will further highlight the effect of actuator dynamics on the wind turbine system operating under realistic loading conditions, and the impact on structural control approaches. The simulations will also explore the effects of gear ratio and controller type in a realistic setting. Simulations using a "pseudo-passive" controller and an $H_\infty$ are analyzed in the following Sections 4.3.1-4.3.2.

### 4.3.1 Pseudo-Passive Analysis

In order to run FAST simulations using actuator models, an updated control module is integrated with the FAST Simulink interface. Since the previous work on active controller design used a complex $H_\infty$ controller, a "pseudo-passive" simulation is run initially to isolate the effects of CSI on performance. In the pseudo-passive simulations, the force that the passive spring and damper would apply to the mass is used as the control force value for the actuator. This system is essentially mimicking a simple PD controller, with the spring constant as the proportional constant, and the damping value as the derivative constant.

Due to the effect of different gear ratios that was shown in the frequency analysis in Figure 4.3, high and low gear ratio values are used in the simulations. The FAST-SC simulations are run for 600 seconds with all turbine degrees of freedom turned on in order to simulate a realistic senario. This includes all platform motions, all tower and blade bending modes, rotor aerodynamic calculations and loading, and wave loading. Two different wind input files are generated by TurbSim, a subroutine that produces full-field turbulent wind data. The two wind files used have average speeds of 10 m/s (below-rated) and 18 m/s (above-rated) and use the IEC Normal Turbulence Model. The wave loading used has a significant wave height of 2.3 m for the 10 m/s wind speed simulations and 3.7 m for the 18 m/s simulations. The peak spectral period for these wave inputs were 14 s, and the waves are constructed using the Jonswap spectrum. This wave loading represents relatively rough seas. It should also be noted that in all simulations in this chapter, no position constraints on the HMD mass are utilized. In some cases this results in unrealistically large displacements, but for the purposes of analyzing the effects of CSI, this issue can be ignored.

In order to select the gear ratios to be used, preliminary testing is carried out, and it is found that gear ratios higher than 10 rad/m resulted in controller instabilities

with the motor model that is used. Therefore, the high gear ratio is selected to be 6.67 rad/m, and the low gear ratio is 2.5 rad/m.

Comparisons of major structural performance metrics for the pseudo-passive simulation to the baseline passive system can be seen in Table 4.4. The metrics used for the pseudo-passive simulation to quantify performance include: blade root flapwise damage equivalent load (DEQL), tower fore-aft DEQL, low speed shaft (LSS) DEQL, RMS platform pitch angle, RMS actuator power, RMS HMD displacement, and RMS Fore-Aft Tower Top displacement. The damage equivalent loads are fatigue loads calculated using a rainflow counting method. This method uses a one Hertz equivalent load and uses a Wohler exponent of 10 for fiberglass and 3 for steel components. Minimizing the tower fatigue loads is the goal of this research, so tower fore-aft DEQL is one of the more important metrics.

| Performance Index | Passive 18 m/s | Low Gear Ratio | High Gear Ratio |
|---|---|---|---|
| Flap DEQL [kNm] | 12326 | 12194 | 11348 |
| % Improvement from passive | - | 1.1% | 7.9% |
| Tower Fore-Aft DEQL [kNm] | 53307 | 52674 | 48501 |
| % Improvement from passive | - | 1.2% | 9.0% |
| LSS DEQL [kNm] | 990 | 979 | 927 |
| % Improvement from passive | - | 1.2% | 6.4% |
| RMS Platform Pitch Angle [deg] | 2.50 | 2.46 | 2.19 |
| % Improvement from passive | - | 1.7% | 12.7% |
| Mean Actuator Power [kW] | 0 | 28.7 | 36.7 |
| % Improvement from low | - | - | -27.9% |
| RMS AMD Displacement [m] | 2.99 | 3.40 | 8.01 |
| % Improvement from passive | - | -13.5% | -167.6% |
| RMS Fore-Aft Tower Top Displacement [m] | 0.507 | .503 | 0.467 |
| % Improvement from passive | - | 1.0% | 8.02% |

**Table 4.2.** Results of simulation with 18m/s wind and pseudo-passive controller

The results for the 10 m/s wind speed pseudo-passive simulation can be seen in Table 4.3. All of the pseudo-passive simulations indicate that the models that included CSI effects actually demonstrated better performance compared to the baseline passive system in all metrics except actuator power and AMD displacement. This is due to the controller over-correcting the output force, which puts a higher force on the tower top, and reduces accelerations and loads. However, the increased power requirements for the actuator are extreme as the gear ratio is increased, with the

| Performance Index | Passive 10 m/s | Low Gear Ratio | High Gear Ratio |
|---|---|---|---|
| Flap DEQL [kNm] | 6665 | 6520 | 7647 |
| % Improvement from passive | - | 2.2% | -14.7% |
| Tower Fore-Aft DEQL [kNm] | 31868 | 31461 | 43751 |
| % Improvement from passive | - | 1.3% | -37.3% |
| LSS DEQL [kNm] | 556 | 550 | 583.4 |
| % Improvement from passive | - | 1.1% | -5.0% |
| RMS Platform Pitch Angle [deg] | 2.10 | 2.19 | 2.71 |
| % Improvement from passive | - | 0.8% | -23.4% |
| Mean Actuator Power [kW] | 0 | 13.1 | 48.3 |
| % Improvement from low | - | - | -267.3% |
| RMS HMD Displacement [m] | 2.03 | 2.32 | 9.22 |
| % Improvement from passive | - | -14.1% | -354.3% |
| RMS Fore-Aft Tower Top Displacement [m] | 0.476 | 0.475 | .538 |
| % Improvement from passive | - | 0.3% | -12.9% |

**Table 4.3.** Results of simulation with 10m/s wind and pseudo-passive controller

high gear ratio actuator requiring about 2.5 times more power than the low gear ratio system int the 10 m/s wind speed simulation. This trend becomes more apparent when the complex controller is integrated in the next section.

### 4.3.2 HMD Anlysis

Next, simulations are run in order to compare previous work in active control using an ideal actuator with the more realistic actuator model developed here. A family of active controllers was developed by Rotea et al. [27, 33] for this application, but was designed for an ideal actuator in which commanded force equals applied force. A high authority and a low authority controller is selected from this previous work to test with the motor model.

In this section of the results only one representative set of the simulations will be analyzed in depth. The simulations selected have a mean wind speed of 18 m/s and use the high authority controller. The wind and wave inputs used in these simulations are the same as those used in the pseudo-passive analysis. Most of the trends that will be presented with these simulations hold true for the other wind speeds and controllers, however, for low authority controllers in below rated conditions, the high gear ratio actuator performs worse in all performance indices. This can be seen in Table 4.7.

Table 4.4 shows the results of the four control schemes at 18 m/s windspeed using the high authority controller. As in the pseudo-passive simulations, the actuator models that include CSI preform better than the ideal controller in most metrics. Once again, the extra force from the CSI reduces tower top acceleration, and thus loading. However, this extra force requires substantially more actuation power, with the high gear ratio motor requiring over 5 times as much power as the ideal motor. A plot of a one minute section of actuation power can be seen in Figure 4.4. Tables 4.5-4.7 show the three other wind and controller combinations resulting from the analysis.

| Performance Index | Passive 18 m/s | Ideal Actuator High Authority | Low Gear Ratio High Authority | High Gear Ratio High Authority |
|---|---|---|---|---|
| RMS Power Error [kW] | 199 | 160 | 156 | 142 |
| % Improvement from passive | - | 19.6% | 21.5% | 28.9% |
| RMS Rotor Speed Error [rpm] | 1.25 | 1.10 | 1.09 | 1.02 |
| % Improvement from passive | - | 12.3% | 13.6% | 18.8% |
| Flap DEQL [kNm] | 12326 | 10949 | 10853 | 10586 |
| % Improvement from passive | - | 11.1% | 12.0% | 14.1% |
| Tower Fore-Aft DEQL [kNm] | 53307 | 44090 | 43557 | 40963 |
| % Improvement from passive | - | 17.3% | 18.3% | 23.2% |
| LSS DEQL [kNm] | 990 | 916 | 909 | 882 |
| % Improvement from passive | - | 7.5% | 8.2% | 10.9% |
| RMS Platform Pitch Angle [deg] | 2.50 | 2.12 | 2.08 | 1.98 |
| % Improvement from passive | - | 15.5% | 17.0% | 20.8% |
| Mean Actuator Power [kW] | 0 | 253.2 | 308.7 | 1517.2 |
| % Improvement from ideal | - | - | -21.9% | -499.0% |
| RMS HMD Displacement [m] | 2.99 | 6.54 | 7.07 | 13.8 |
| % Improvement from passive | - | -118.4% | -136.0% | -360.1% |
| RMS Fore-Aft Tower Top Displacement [m] | 0.507 | 0.455 | 0.450 | 0.434 |
| % Improvement from passive | - | 10.3% | 11.4% | 14.5% |

**Table 4.4.** Results of simulation with 18m/s wind and high authority controller

| Performance Index | Passive 18 m/s | Ideal Actuator Low Authority | Low Gear Ratio Low Authority | High Gear Ratio Low Authority |
|---|---|---|---|---|
| RMS Power Error [kW] | 199 | 184 | 180 | 156 |
| % Improvement from passive | - | 7.9% | 9.6% | 21.6% |
| RMS Rotor Speed Error [rpm] | 1.25 | 1.19 | 1.18 | 1.06 |
| % Improvement from passive | - | 5.1% | 6.3% | 15.4% |
| Flap DEQL [kNm] | 12326 | 11755 | 11651 | 10815 |
| % Improvement from passive | - | 4.6% | 5.5% | 12.3% |
| Tower Fore-Aft DEQL [kNm] | 53307 | 48842 | 48305 | 44448 |
| % Improvement from passive | - | 8.4% | 9.4% | 16.6% |
| LSS DEQL [kNm] | 990 | 955 | 949 | 899 |
| % Improvement from passive | - | 3.6% | 4.2% | 9.2% |
| RMS Platform Pitch Angle [deg] | 2.50 | 2.34 | 2.30 | 2.08 |
| % Improvement from passive | - | 6.4% | 7.8% | 17.0% |
| RMS Actuator Power [kW] | 0 | 61.9 | 84.3 | 709.0 |
| % Improvement from ideal | - | - | -36.3% | -1045.1% |
| RMS HMD Displacement [m] | 2.99 | 4.28 | 4.65 | 9.81 |
| % Improvement from passive | - | -42.9% | -55.3% | -227.6% |
| RMS Fore-Aft Tower Top Displacement [m] | 0.507 | 0.485 | 0.480 | 0.449 |
| % Improvement from passive | - | 4.5% | 5.4% | 11.6% |

**Table 4.5.** Results of simulation with 18m/s wind and low authority controller

| Performance Index | Passive 10 m/s | Ideal Actuator Low Authority | Low Gear Ratio Low Authority | High Gear Ratio Low Authority |
|---|---|---|---|---|
| Flap DEQL [kNm] | 6665 | 6038 | 6041 | 5959 |
| % Improvement from passive | - | 9.4% | 9.4% | 10.6% |
| Tower Fore-Aft DEQL [kNm] | 31868 | 24811 | 24429 | 22346 |
| % Improvement from passive | - | 22.1% | 23.3% | 29.9% |
| LSS DEQL [kNm] | 556 | 514 | 520 | 519 |
| % Improvement from passive | - | 7.5% | 6.5% | 6.7% |
| RMS Platform Pitch Angle [deg] | 2.10 | 2.03 | 2.01 | 1.95 |
| % Improvement from passive | - | 8.0% | 8.7% | 11.4% |
| Mean Actuator Power [kW] | 0 | 126.1 | 154.1 | 769.3 |
| % Improvement from ideal | - | - | -22.1% | -509.9% |
| RMS HMD Displacement [m] | 2.03 | 4.56 | 4.93 | 9.75 |
| % Improvement from passive | - | -124.4% | -143.0% | -380.4% |
| RMS Fore-Aft Tower Top Displacement [m] | 0.476 | 0.457 | 0.455 | 0.449 |
| % Improvement from passive | - | 4.1% | 4.5% | 5.8% |

**Table 4.6.** Results of simulation with 10m/s wind and high authority controller

| Performance Index | Passive 10 m/s | Ideal Actuator Low Authority | Low Gear Ratio Low Authority | High Gear Ratio Low Authority |
|---|---|---|---|---|
| Flap DEQL [kNm] | 6665 | 6377 | 6356 | 7343 |
| % Improvement from passive | - | 4.3% | 4.6% | -10.2% |
| Tower Fore-Aft DEQL [kNm] | 31868 | 28462 | 28245 | 40123 |
| % Improvement from passive | - | 10.7% | 11.4% | -25.9% |
| LSS DEQL [kNm] | 556 | 542 | 538 | 575 |
| % Improvement from passive | - | 2.4% | 3.2% | -3.4% |
| RMS Platform Pitch Angle [deg] | 2.10 | 2.14 | 2.13 | 2.61 |
| % Improvement from baseline | - | 2.9% | 3.5% | -18.6% |
| Mean Actuator Power [kW] | 0 | 29.3 | 40.2 | 982.8 |
| % Improvement from ideal | - | - | -37.1% | -3247.8% |
| RMS HMD Displacement [m] | 2.03 | 2.96 | 3.23 | 11.69 |
| % Improvement from passive | - | -45.8% | -59.0% | -475.6% |
| RMS Fore-Aft Tower Top Displacement [m] | 0.476 | 0.468 | 0.466 | .522 |
| % Improvement from passive | - | 1.8% | 2.0% | -9.5% |

**Table 4.7.** Results of simulation with 10m/s wind and low authority controller

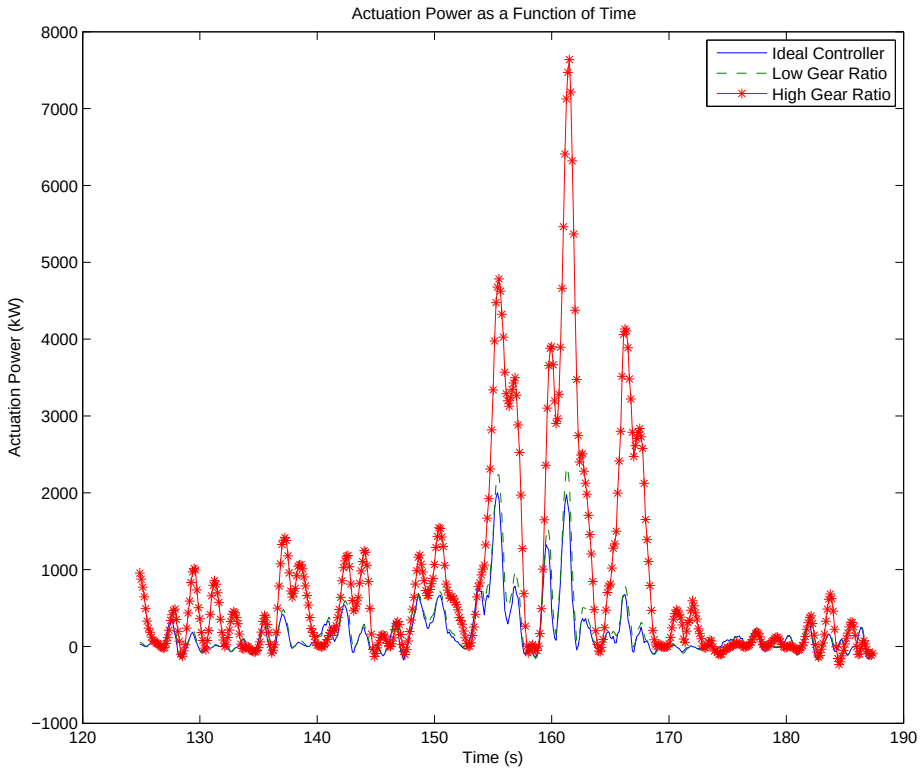


**Figure 4.4.** Actuator power over time for 18 m/s wind and high control authority.

The large increase in power consumption results in a small improvement in tower top displacement, which is evident when comparing Tower Fore-Aft DEQL for the different control schemes. The high gear ratio actuator uses almost 500% more power than the ideal actuator case while decreasing fatigue loading by only 6%.

One important result is that the low gear ratio simulation is similar in performance to the ideal actuator case. This is due to the nearly flat gain in the motor transfer function for low gear ratios (see Figure 4.3). The result is that when designing a structural control system, there is a clear benefit to using low gear ratios, so as to minimize the effect of CSI. The practical effect of changing the gear ratio is changing the rotational speed and torque of the motor. Depending on the motor selected, gear

ratios as low as the ones used in these simulations may result in torque outputs that are too high for continuous duty operation.

# CHAPTER 5

# CONCLUSIONS AND FUTURE WORK

Tuned mass dampers show great promise for use in offshore wind turbines. Both passive and active TMDs can reduce tower and mooring line loads significantly, which leads to lighter and less expensive structures. This thesis contributes a set of optimized passive TMDs for four offshore wind turbines, as well as an analysis of an active controller for the barge platform.

The optimization of the passive tuned mass damper is completed for the monopile, barge, spar buoy, and tension leg platform in Chapter 3. This chapter includes the optimization of the spring and damping parameters using a genetic algorithm. The results of this genetic algorithm are then simulated in FAST-SC and compared to a baseline without a TMD. Each of the four platforms has a unique TMD configuration that results in the best load reduction.

The monopile achieves the best load reduction with both a fore-aft and a side-side TMD in the nacelle. With this configuration, fore-aft loads are reduced by up to 10%, and side-side fatigue loading is reduced by as much as 66%. Side-side ultimate loads are effected as well, with the 95th percentile load being reduced by 32%. The barge benefits from the same TMD configuration, with a 15% fore-aft fatigue damage reduction and up to a 33% reduction in side-side fatigue loading. Even with the load reduction, the best barge fatigue damage values are approximately 4 times the baseline for the monopile.

For the spar buoy, the best configuration involves a nacelle-based TMD as well. With the TMD in the platform, low value of the spring constant combined with

the thrust forcing on the turbine rotor caused the TMD to rest against the stop and contribute very little load reduction. The nacelle-based TMD reduced fore-aft damage by as much as 8%, and side-side fatigue loads by 38%. Ultimate tower loads, however, were increased with the nacelle based TMD. This could be caused by the extra tower top mass from the TMD causing more tower bending due to gravitational and inertial loading in the extremes of the pitching motion.

The TLP was a complex structure to model; the genetic algorithm that was used for the other platforms could not be used for the TLP. However, the parametric study method that was used instead allowed a primary investigation into the effects of a TMD. Since the surge motion of the TLP has the largest amplitude of the platform DOFs, this was initially assumed to have the largest effect on tower loading. Preliminary investigations showed that although a surge-tuned TMD reduces the amplitude of this motion, it does little to effect tower or mooring line loading. The platform pitching motion was found to influence both tower bending and line tension the most, so a TMD was developed to reduce this motion for use in the platform and nacelle. The nacelle based TMD once again proved to have a better effect on loading than the TMD in the platform. The nacelle TMD reduced tower fore-aft loads by almost 8%, and side-side loads by 21%. The TMD had little effect on fore-aft ultimate loads, but reduced side-side peak loads by 7%. Line loading was also effected; the TMD reduced line fatigue damage by 7%.

In Chapter 4, a design of an active control system for a mass damper in an offshore wind turbine using the barge floating platform is modified to include an actuator model. The addition of the actuator model creates a more realistic simulation, and motivates a controller redesign. When the actuator is added, the AMD uses 5-10 times more power in some cases, while reducing loads by only a few percent. In order to make an active controller viable for offshore wind turbines, actuator models must be included in future work.

These load reductions for all of the platforms could have a beneficial effect on the cost of an offshore wind turbine as long as the TMD could be constructed at a reasonable cost. Future work on this topic should consider a preliminary economic feasibility study. This study should quantify the cost associated with the load reduction and compare this to the material and construction cost of a TMD, as well as the power usage in the case of an AMD.

## 5.1 Other TMD Research Topics for Investigation

### 5.1.1 TLCD

All of the studies in this thesis focused on using an ideal tuned mass damper. In practice, however, the mechanics of a tuned mass damper may be difficult to achieve. For example, with a stroke of ±8m, a spring would need to stretch 16m and a spring like this may not exist, or may prohibitively expensive. A tuned liquid column damper may be a good alternative to the tuned mass damper for this application. The water which supplies the mass in a TLCD is essentially free for an offshore turbine, and there are no large scale springs and dampers involved. Further research should go into developing a passive TLCD for use in an offshore wind turbine.

### 5.1.2 Semi-Active

Another topic that should be investigated is a semi-active damper. With a proper control scheme, these devices have been shown to approach AMDs in terms of load reduction with minimum power requirements. A controllable orifice TLCD is also a promising alternative. This modification to the TLCD allows for semi-active control in addition to the other benefits of the TLCD.

### 5.1.3 Redesigned HMD

Due to the findings from the CSI study and the passive optimization study, the HMD that was developed for the barge should be altered, and HMDs should be

developed for the remaining platforms. The controller itself needs to be redesigned taking actuator dynamics into consideration. Also, the original spring and damping constants for the HMD were taken from the parametric study, and the improved parameters should be used to achieve the optimum system.

## 5.2 Concluding Remarks

Tuned mass dampers have great potential to be used in offshore wind turbines. All of the floating platforms and the fixed bottom platform analyzed in this thesis showed improvement in fatigue damage with the application of both active and passive tuned mass dampers. A few problems still need to be addressed to make mass dampers practical for floating wind turbines. Due to the cost and manufacturing challenges of constructing a tuned mass damper for this application, alternative forms of mass damper systems including tuned liquid column dampers should be considered. Alternatively, a purely active mass damper should be considered, which would eliminate the need for large displacement springs and dampers. Control-structure interaction must be taken into account when designing this system. With these recommendations, tuned mass dampers could provide a cost effective means of load reduction in offshore wind turbines.

# APPENDIX

# GENETIC ALGORITHM CODE

```
lenk=13;                  % The length of the genomes
lend=15;
popSize=50;               % The size of the population (must be an even number)
maxGens=20;               % The maximum number of generations allowed in a run
probCrossover=.7;           % The probability of crossing over.
probMutation=0.01;         % The mutation probability (per bit)
sigmaScalingFlag=1;        % Sigma Scaling is described on pg 168 of M. Mitchell's
                           % GA book. It often improves GA performance.
sigmaScalingCoeff=.7;       % Higher values => less fitness pressure

SUSFlag=1;                 % 1 => Use Stochastic Universal Sampling (pg 168 of
                           %      M. Mitchell's GA book)
                           % 0 => Do not use Stochastic Universal Sampling
                           %      Stochastic Universal Sampling almost always
                           %      improves performance

crossoverType=1;           % 0 => no crossover
                           % 1 => 1pt crossover
                           % 2 => uniform crossover

visualizationFlag=0;       % 0 => don't visualize bit frequencies
                           % 1 => visualize bit frequencies

verboseFlag=1;             % 1 => display details of each generation
                           % 0 => run quietly

useMaskRepositoriesFlag=1; % 1 => draw uniform crossover and mutation masks from
                           %      a pregenerated repository of randomly generated bits.
                           %      Significantly improves the speed of the code with
                           %      no apparent changes in the behavior of
                           %      the SGA
                           % 0 => generate uniform crossover and mutation
                           %      masks on the fly. Slower.

% crossover masks to use if crossoverType==0.
%mutationOnlycrossmasks=false(popSize,len);

% pre-generate two repositories of random binary digits from which the
% the masks used in mutation and uniform crossover will be picked.
% maskReposFactor determines the size of these repositories.

maskReposFactor=5;
uniformCrossmaskReposk=rand(popSize/2,(lenk+1)*maskReposFactor)<0.5;
uniformCrossmaskReposd=rand(popSize/2,(lend+1)*maskReposFactor)<0.5;
uniformCrossmaskReposm=rand(popSize/2,(lenm+1)*maskReposFactor)<0.5;
mutmaskReposk=rand(popSize,(lenk+1)*maskReposFactor)<probMutation;
mutmaskReposd=rand(popSize,(lend+1)*maskReposFactor)<probMutation;
mutmaskReposm=rand(popSize,(lenm+1)*maskReposFactor)<probMutation;

% preallocate vectors for recording the average and maximum fitness in each
% generation
avgFitnessHist=zeros(1,maxGens+1);
maxFitnessHist=zeros(1,maxGens+1);


eliteIndiv=[];
eliteFitness=-realmax;


% the population is a popSize by len matrix of randomly generated boolean
% values
popk=rand(popSize,lenk)<.5;
popd=rand(popSize,lend)<.5;

for gen=0:maxGens

    % evaluate the fitness of the population. The vector of fitness values
    % returned  must be of dimensions 1 x popSize.
    for c = 1:popSize
            fitnessVals(c)=1/(optimize_sim_bouy([bin2dec(num2str((popk(c,:)))),...
            bin2dec(num2str((popd(c,:))))]));
    end
```

```
[maxFitnessHist(1,gen+1),maxIndex]=max(fitnessVals);
avgFitnessHist(1,gen+1)=mean(fitnessVals);
if eliteFitness<maxFitnessHist(gen+1)
    eliteFitness=maxFitnessHist(gen+1);
    eliteIndivk=popk(maxIndex,:);
    eliteIndivd=popd(maxIndex,:);
end

% display the generation number, the average Fitness of the population,
% and the maximum fitness of any individual in the population
if verboseFlag
    display(['gen=' num2str(gen,'%.3d') '   avgFitness=' ...
        num2str(avgFitnessHist(1,gen+1),'%3.3f') '   maxFitness=' ...
        num2str(maxFitnessHist(1,gen+1),'%3.3f')]);
end

% Conditionally perform sigma scaling
if sigmaScalingFlag
    sigma=std(fitnessVals);
    if sigma~=0;
        fitnessVals=1+(fitnessVals-mean(fitnessVals))/...
        (sigmaScalingCoeff*sigma);
        fitnessVals(fitnessVals<=0)=0;
    else
        fitnessVals=ones(popSize,1);
    end
end


% Normalize the fitness values and then create an array with the
% cumulative normalized fitness values (the last value in this array
% will be 1)
cumNormFitnessVals=cumsum(fitnessVals/sum(fitnessVals));

% Use fitness proportional selection with Stochastic Universal or Roulette
% Wheel Sampling to determine the indices of the parents
% of all crossover operations
if SUSFlag
    markers=rand(1,1)+[1:popSize]/popSize;
    markers(markers>1)=markers(markers>1)-1;
else
    markers=rand(1,popSize);
end
[temp parentIndices]=histc(markers,[0 cumNormFitnessVals]);
parentIndices=parentIndices(randperm(popSize));

% deterimine the first parents of each mating pair
firstParentsk=popk(parentIndices(1:popSize/2),:);
firstParentsd=popd(parentIndices(1:popSize/2),:);
% determine the second parents of each mating pair
secondParentsk=popk(parentIndices(popSize/2+1:end),:);
secondParentsd=popd(parentIndices(popSize/2+1:end),:);

% create crossover masks
if crossoverType==0
    masks=mutationOnlycrossmasks;
elseif crossoverType==1
    masksk=false(popSize/2, lenk);
    masksd=false(popSize/2, lend);
    tempk=ceil(rand(popSize/2,1)*(lenk-1));
    tempd=ceil(rand(popSize/2,1)*(lend-1));
    for i=1:popSize/2
        masksk(i,1:tempk(i))=true;
        masksd(i,1:tempd(i))=true;
    end
else
    if useMaskRepositoriesFlag
        tempk=floor(rand*lenk*(maskReposFactor-1));
        tempd=floor(rand*lend*(maskReposFactor-1));
        masksk=uniformCrossmaskReposk(:,tempk+1:tempk+lenk);
        masksd=uniformCrossmaskReposd(:,tempd+1:tempd+lend);
    else
        masksk=rand(popSize/2, lenk)<.5;
        masksd=rand(popSize/2, lend)<.5;
    end
end

% determine which parent pairs to leave uncrossed
reprodIndices=rand(popSize/2,1)<1-probCrossover;
masksk(reprodIndices,:)=false;
masksd(reprodIndices,:)=false;

% implement crossover
firstKidsk=firstParentsk;
firstKidsd=firstParentsd;
firstKidsk(masksk)=secondParentsk(masksk);
firstKidsd(masksd)=secondParentsd(masksd);
secondKidsk=secondParentsk;
secondKidsd=secondParentsd;
secondKidsk(masksk)=firstParentsk(masksk);
secondKidsd(masksd)=firstParentsd(masksd);
popk=[firstKidsk; secondKidsk];
```

```
    popd=[firstKidsd; secondKidsd];

    % implement mutation
    if useMaskRepositoriesFlag
        tempk=floor(rand*lenk*(maskReposFactor-1));
        tempd=floor(rand*lend*(maskReposFactor-1));
        masksk=mutmaskReposk(:,tempk+1:tempk+lenk);
        masksd=mutmaskReposd(:,tempd+1:tempd+lend);
    else
        masksk=rand(popSize, lenk)<probMutation;
        masksd=rand(popSize, lend)<probMutation;
    end
    popk=xor(popk,masksk);
    popd=xor(popd,masksd);
end
if verboseFlag
    figure(2)
    %set(gcf,'Color','w');
    hold off
    plot([0:maxGens],avgFitnessHist,'k-');
    hold on
    plot([0:maxGens],maxFitnessHist,'c-');
    title('Maximum and Average Fitness')
    xlabel('Generation')
    ylabel('Fitness')
end
```

# BIBLIOGRAPHY


[1] Adeli, H. Smart structures and building automation in the 21st century. In *The 25th International Symposium on Automation and Robotics in Construction* (June 2008).

[2] Adeli, H., and Saleh, A. Integrated structural/control optimization of large adaptive/smart structures. *International Journal of Solids and Structures 35*, 28-29 (1998), 3815 – 3830. Active control systems;Parallel vector algorithms;.

[3] Alves, R.M., and Batista, R.C. Active/passive control of heave motion for tlp type offshore platform. In *International Conference on Offshore Mechanics and Arctic Engineerings* (1999), pp. 332–338.

[4] Battaini, M., Yang, G., and Spencer, B.F. Bench-scale experiment for structural control. *Journal of Engineering Mechanics 126*, 2 (2000), 140–148.

[5] Butterfield, S., Musial, W., Jonkman, J., and Sclavounos, P. Engineering challenges for floating offshore wind turbines. In *Copenhagen Offshore Wind Conference* (Copenhagen, Denmark, October 2005), pp. 377–382.

[6] Calderon, B.E. Design and optimization of a wind turbine tower by using a damper device. Master's thesis, Stuttgart University, 2009.

[7] Colwell, S., and Basu, B. Tuned liquid column dampers in offshore wind turbines for structural control. *Engineering Structures 31*, * (2009), 358–368.

[8] Dyke, S.J., Spencer, B.F., Quast, P., and Sain, M.K. The role of control-structure interaction in protective system design. *Journal of Engineering Mechanics 121*, 2 (1995), 322–338.

[9] Dyke, S.J., Spencer, B.F., Quast, P., Sain, M.K., Kaspari, D.C., and Soong, T.T. Experimental verification of acceleration feedback control strategies for an active tendon system. Tech. Rep. NCEER-94-0024, National Center for Earthquake Engineering Research, 1994.

[10] Enevoldsen, I. Effects of a vibration mass damper in a wind turbine tower. *Mechanics of Structures and Machines 24*, 2 (1996), 155–187.

[11] EWEA. Upwind: Design limits and solutions for very large wind turbines. Tech. rep., EWEA, March 2011.

[12] Fujita, T. Application of hybrid mass damper with convertible active and passive modes using hydraulic actuator to high-rise building. In *American Control Conference* (Baltimore, Maryland, June 1994).

[13] Gao, H., and Kwok, K.C.S. Optimization of tuned liquid column dampers. *Engineering Structures 19*, 6 (1997), 476–486.

[14] Hirayama, T., and Ma, N. Dynamic response of a very large floating structure with active pneumatic control. In *7th International Offshore and Polar Engineering Conference* (Honolulu, Hawaii, May 1997), pp. 377–382.

[15] International Electrotechnical Commission 614003:2008. *Wind Turbines–Part 3: Design Requirements for Offshore Wind Turbines*. International Electrotechnical Commission, Geneva, Switzerland.

[16] Jonkman, B.J., and Buhl, M. L. Turbsim user's guide. Tech. Rep. NREL/EL-500-36970, National Renewable Energy laboratory, Golden, Colorado, 2005.

[17] Jonkman, J. *Dynamics Modeling and Loads Analysis of an Offshore Floating Wind Turbine*. PhD thesis, National Renewable Energy Laboratory, 2008.

[18] Jonkman, J. Influence of control on the pitch damping of a floating wind turbine. In *46th AIAA Aerospace Science Meeting and Exhibit* (Reno, Nevada, January 2008).

[19] Jonkman, J., and Buhl, M. L. Fast user's guide. Tech. Rep. NREL/EL-500-38230, National Renewable Energy laboratory, Golden, Colorado, 2006.

[20] Jonkman, J., Butterfield, S., Musial, W., and Scott, G. Definition of a 5-mw reference wind turbine for offshore system development. TP 500-38060, National Renewable Energy Laboratory, 2008.

[21] Jonkman, J., and Matha, D. A quantitative comparison of the responses of three floating platform concepts. In *European Offshore Wind 2009 Conference and Exhibition* (Stockholm, Sweden, September 2009).

[22] Kanegaonkar, H.B. Smart technology systems in offshore structures: Status and needs. In *9th International Offshore and Polar Engineering Conference* (Brest, France, May 1999).

[23] Krenk, S. Frequency analysis of the tuned mass damper. *ASME Journal of Applied Mechanics 72* (November 2005), 936– 942.

[24] Krenk, S., and Høgsberg, Jan. Tuned mass absorbers on damped structures under random load. *Probabilistic Engineering Mechanics 23* (2008), 408– 415.

[25] Kusko, A. *Solid-State DC Motor Drives*. The M.I.T. Press, Cambridge, Massachusetts, 1969.

[26] Lackner, M.A. An investigation of the control and loads of floating wind turbines. *Under Review, Wind Energy*, 4 (2009), 1118–1142.

[27] Lackner, M.A., and Rotea, M. Structural control of floating wind turbines. *Mechatronics* (2010). In press, available online.

[28] Lackner, M.A., and Rotea, M.A. Passive structural control of offshore wind turbines. *Wind Energy* (September 2010). DOI: 10.1002/we.426.

[29] Lee, H.H., Wong, S.H., and Lee, R.S. Response mitigation on the offshore floating platform system with tuned liquid column damper. *Ocean Engineering 33*, 4 (2006), 1118–1142.

[30] Murtagh, P.J., Ghosh, A., Basu, B., and Broderick, B.M. Passive control of wind turbine vibrations including blade/tower interaction and rotationally sampled turbulence. *Wind Energy 11*, 4 (2007), 305–317.

[31] Musial, W., Butterfield, S., and Ram, B. Energy from offshore wind. In *Offshore Technology Conference* (Houston, Texas, May 2006).

[32] Nagashima, I., Maseki, R., Asami, Y., Hirai, J., and Abiru, H. Performance of hybrid mass damper system applied to a 36-storey high-rise building. *Earthquake Engineering and Structural Dynamics 30* (2001), 1615–1637.

[33] Rotea, M.A., Lackner, M.A., and Saheba, R. Active structural control of offshore wind turbines. In *48th AIAA Aerospace Science Meeting and Exhibit* (Orlando, Florida, January 2010).

[34] Singh, M.P., and Matheu, E.E. Active and semi-active control of structures under seismic excitation. *Earthquake Engineering and Structural Dynamics 26* (1997), 193–213.

[35] Soong, T.T., and Spencer, B.F. Supplemental energy dissipation: state-of-the-art and state-of-the practice. *Engineering Structures 24* (2002), 243–259.

[36] Spencer, B.F., and Nagarajaiah, S. State of the art of structural control. *Journal of Structural Engineering 129*, 7 (2003), 845–856.

[37] Spencer, B.F., and Sain, M.K. Controlling buildings - a new frontier in feedback. *The Shock and Vibration Digest 30*, 4 (1998), 267–281.

[38] Symans, M.D., and Constantinou, M.C. Semi-active control systems for seismic protection of structures: A state-of-the-art review. *Engineering Structures 21*, * (1999), 469–487.

[39] Wilmink, A.J., and Hengeveld, J.F. Application of tuned liquid column dampers in wind turbines. Tech. rep., Mecal Applied Mechanics, Netherlands, 2006.

[40] Yamanaka, M., and Okuda, H. Dentsu head office damping systems, tokyo, japan. *Structural Engineering International 15*, 1 (2005).